Advanced Composites and Hybrid Materials (2023) 6:104
https://doi.org/10.1007/s42114-023-00673-w

RESEARCH

Novel strategy of senescence elimination via toxicity-exempted kinome perturbations by nanoliposome-based thermosensitive hydrogel for osteoarthritis therapy

Junlai Wan[1] · Zhiyi He[1] · Yingchao Zhao[2,3] · Xiaoxia Hao[4] · Jiarui Cui[5] · Anmin Chen[1] · Jun Zhou[6,7] · Jiaming Zhang[1]

Received: 17 March 2023 / Revised: 14 April 2023 / Accepted: 18 April 2023 / Published online: 18 May 2023

Abstract

Cellular senescence and the senescence-associated secretory phenotype (SASP) have been implicated in osteoarthritis (OA). This study aims to determine whether multi-kinase inhibitor YKL-05-099 (Y099) has potential in senescence elimination and OA therapy and whether delivering Y099 by nanoliposmal hydrogel improves the performance of the kinase inhibitor. Y099 inhibited IL-1β-induced inflammation and catabolism and promoted anabolism of chondrocytes. To attenuate the inhibition of cell viability, nanoliposomal Y099-loaded thermosensitive hydrogel (Y099-Lip-Gel) was developed for sustained release and toxicity exemption. Notably, Y099-Lip-Gel exhibited a pronounced effect on promoting anabolism and suppressing catabolism and inflammation without causing the inhibition of chondrocyte viability. Moreover, Y099-Lip-Gel remarkably increased the master regulator of chondrocyte phenotype *Sox9* expression. After four intra-articular injections of Y099-Lip-Gel in the OA murine model, the histological lesions of cartilage were attenuated by Y099-Lip-Gel with subchondral bone loss and osteoclast formation inhibited. Transcriptomic analysis and experimental validations revealed that Y099-Lip-Gel suppressed cellular senescence by inhibiting the expression of senescence inducers and SASP factors. Furthermore, the phosphoproteomic analysis showed that Y099-Lip-Gel exerted a significant influence on kinome phosphorylation, inhibiting the MAPK and NF-κB signaling activations. The protective effects of Y099-Lip-Gel were also validated in cultured human OA cartilage explants. In conclusion, nanoliposomal Y099-loaded thermosensitive hydrogel has considerable potential in OA therapy. Nanoliposome-based hydrogel system has strength in reducing kinase inhibition-induced cytotoxicity, enhancing cellular tolerance to kinome perturbation, and improving the performance of protein kinase inhibitors. Senescence elimination via toxicity-exempted kinome perturbations achieved by advanced nanotechnology is a promising strategy for OA.

Keywords Osteoarthritis · Cellular senescence · Protein kinase · Nanoliposome · Hydrogel

1 Introduction

Osteoarthritis (OA) is a common age-related degenerative joint disease, characterized by progressive articular cartilage degradation, synovial inflammation, osteophyte formation, subchondral bone lesions, and abnormal angiogenesis, which causes chronic pain, swelling, stiffness, and motion restriction [1, 2]. Due to the high incidence, the absence of effective therapy for early OA, and the high cost of joint replacement for advanced OA, OA has become a worldwide challenge. Recent research advances in the mechanisms of OA have promoted the understanding of this disease and indicated some novel therapies based on these findings, which may be promising for OA therapy. Cellular senescence has been implied in a wide range of age-related diseases, including OA [3, 4]. As a hallmark of aging, accumulated cellular senescence is a permanent state of cell-cycle arrest accompanied by the release of a group of pro-inflammatory cytokines, chemokines, matrix metalloproteases (MMPs), and growth factors with autocrine, paracrine, and endocrine activities, which is a senescence-related secretome termed

Junlai Wan, Zhiyi He, and Yingchao Zhao contributed equally to this work.

✉ Anmin Chen
anminchen@hust.edu.cn

✉ Jun Zhou
zhoujun@dent.showa-u.ac.jp

✉ Jiaming Zhang
jiaming_zhangtjmc@icloud.com

Extended author information available on the last page of the article

senescence-associated secretory phenotype (SASP) [5]. Cellular senescence is caused by oxidative stress, DNA damage, and dysfunctional oncogenes, contributing to inflammation, the decline of the tissue regenerative potential and function, and tumorigenesis [6]. Due to the intrinsic relationship between cellular senescence and aging and aging-related inflammation, targeting senescence is a promising novel strategy for OA therapy.

Kinome is a collection that comprises 538 kinases playing critical functions by catalyzing protein phosphorylation and regulating intracellular signaling events [7]. Due to the critical roles of protein kinases in the mechanisms of diseases, such as inflammation [8] and aging [9], small molecule kinase inhibitors have been introduced into research and approved for clinical applications [10]. Multiple kinases and related signaling pathways, such as the mitogen-activated protein kinase (MAPK) pathway and NF-κB pathway, have also been implied in reactive oxygen species (ROS) or mechanical stress-induced cellular senescence and the SASP productions in OA [11, 12]. Although the experimental findings have demonstrated the potential of targeting kinases in OA [13, 14], kinase-based targeting strategies have not been fully established in OA therapy due to the challenges in improving target selectivity and attenuating toxicity associated with off-target effects [8]. YKL-05-099 (Y099) is a novel multi-kinase kinase inhibitor that increases bone formation without increasing bone resorption by dual-targeting salt-inducible kinases and CSF1R in the experimental osteoporosis model [15, 16]. Since subchondral bone is an essential element supporting cartilage and the subchondral bone loss has been characterized as an early OA change [17], Y099 may be promising in targeting the subchondral bone to prevent OA progress. Furthermore, Y099 has been shown to inhibit tyrosine kinases, which have been identified as promising drug targets for OA [16, 18]. However, the cytotoxicity of Y099 has also been suggested since it can be used as a chemotherapy agent in cancer therapy [19]. Thus, the effects and potential of Y099 in OA therapy remain unclear.

Nanotechnology and nanomedicine have become fields full of potential and prospects [20–27]. Nanotechnology-based delivery systems are efficacy in reducing toxicity and improving the performance of the encapsulated drugs [28, 29]. Numerous emerging nanoliposomes, micelles, dendrimers, polymeric nanoparticles, exosomes, and inorganic nanoparticles have shown their potential in drug delivery to facilitate the effective therapy of OA [30]. Moreover, injectable hydrogels can improve the retention of nanoscale drug vehicles in joints and further prolong the sustained drug release without causing toxicity [31]. In this context, we assumed that Y099 could attenuate OA progress by regulating kinome and eliminating cellular senescence, and encapsulating Y099 in nanoliposomes loaded in hydrogel could effectively reduce toxicity and improve cellular tolerance to kinome perturbations of Y099, by sustained release. In the present study, nanoliposomal Y099-loaded thermosensitive hydrogel was developed and assessed in OA therapy. Using a series of cutting-edge and high-throughput technologies, this study revealed for the first time the therapeutic potential and mechanisms of Y099, such as senescence elimination and inflammation suppression, in OA. More importantly, this study demonstrated the strength of nanoliposome-based hydrogel delivery system in improving the beneficial effects of protein kinase inhibitors. Finally, the findings in human OA cartilage supported the translational value of nanoliposomal Y099-loaded thermosensitive hydrogel.

2 Materials and methods

2.1 Reagents and antibodies

Y099 (CAS 1936529-65-5) was purchased from Topscience (#T17271, China). Recombinant mouse IL-1β (#401-ML) protein and human IL-1β (#201-LB) protein was purchased from R&D Systems (USA). The primary antibodies against matrix metallopeptidase 13 (MMP-13; #18165–1-AP), aggrecan (#13880–1-AP), type II collagen (COL-2; #28459-1-AP), inducible nitric oxide synthase (iNOS; #22226-1-AP), and glyceraldehyde 3-phosphate dehydrogenase (GAPDH; #60004-1-Ig) were purchased from Proteintech Group (China). The primary antibodies against matrix metallopeptidase 3 (MMP-3; #BM4074) and SRY-box transcription factor 9 (SOX9; #A00177-2) were purchased from Boster Biological Technology (China). The primary antibodies against cyclooxygenase 2 (COX2; #12282), ERK1/2 (#4695), Phospho-ERK (#4370), JNK (#9258), Phospho-JNK (#9255), p65 (#8242), Phospho-p65 (#3033), IKKα (#11930), IKKβ (#8943), and Phospho-IKKα/β (#2697) were purchased from Cell Signaling Technology (USA). The primary antibodies against $P21^{Cip1}$ (#ab188224) were purchased from Abcam (China). The $P16^{INK4A}$ antibody (#A0262) was purchased from ABclonal (China). Fetal bovine serum (FBS; #10100147) and Dulbecco's modified Eagle's medium F12 (DMEM/F12) were purchased from Gibco (USA). Collagenase type II, trypsin (0.25%), phosphate buffer saline (PBS), and the secondary antibodies for western blot and immunofluorescence analyses were purchased from Boster Biological Technology (China).

2.2 Preparation and characterization of Y099-loaded nanoliposomes

Y099-loaded nanoliposomes were prepared using the thin film evaporation method. Briefly, 1 mg of Y099, 1 mg of cholesterol (Sigma, USA), and 8 mg of phospholipids (Avanti, USA) were dissolved in a round-bottom flask

containing chloroform. The solution was then rotated and evaporated to form a lipid film. Then, the thin film was dissolved in deionized water under ultrasonic conditions in a water bath and extruded through polycarbonate membranes with pore sizes of 400, 200, and 100 nm to obtain Y099-loaded nanoliposomes, which were lyophilized for later use. To prepare Cy5-labeled Y099-loaded nanoliposomes, Cy5 dye (Thermo Fisher Scientific, USA) was additionally added at a mass fraction of 0.5% using the same method described above. After Y099-loaded nanoliposomes were diluted 1:100 with pure water, the particle size of the nanoliposomes was determined using a Malvern Mastersizer 3000 (Malvern Panalytical, UK). The morphologies of nanoliposomes were investigated using transmission electron microscopy (TEM) (JEOL 2010, Japan).

2.3 Preparation and characterization of nanoliposome-loaded thermosensitive hydrogel

The thermosensitive hydrogel with a mass fraction of 25% and a phase transition temperature of ~ 35 ℃ was prepared using PLGA1500-PEG1200-PLGA1500 polymers (SunLipo NanoTech, China) dissolved in pure water by stirring at 4 ℃. Next, a certain amount of lyophilized Y099 nanoliposomes (w/w = 3%, drug concentration = ~ 3 mg/mL) was added to the gel and dispersed uniformly using low-temperature vortexing to produce a temperature-sensitive and sustained-release water-based hydrogel loaded with Y099 nanoliposomes (Y099-Lip-Gel). Additionally, the hydrogels containing 3% Y099 nanoliposomes or not were lyophilized, placed onto the adhesive tape, vacuum-dried, and sputter-coated with gold before observing the distribution of drug nanoliposomes in the gel under a scanning electron microscope (SEM) (Gemini 300, Zeiss, German). Y099-Lip-Gel was diluted with different volumes of pure water to prepare the solutions with concentrations of 10%, 13%, 16%, 19%, 22%, and 25%. The solutions were heated from 20 to 65 ℃ in a constant temperature water bath. The precipitation-gel-solution phase transition temperature values of Y099-Lip-Gel were measured, and a phase transition diagram was plotted. The modulus-temperature relationship and the modulus-time relationship (37 ℃) of Y099-Lip-Gel (25 wt%) were subsequently measured to obtain gelation temperature and gelation time (37 ℃). The thermal stability of Y099-Lip-Gel was analyzed by a thermogravimetric analyzer TGA 550 (TA Instruments, USA). The samples were heated to 800 °C at the rate of 5 °C/min. In vitro release of drugs of Y099-Lip-Gel was detected by high-performance liquid chromatography (HPLC). Ten-microliter PBS, Cy5-labeled nanoliposomes, hydrogel, or hydrogel loaded with Cy5-labeled nanoliposomes were administrated by intra-articular injections to check the joint retention using Bruker MI fluorescence imaging system with the excitation at 650 nm and the emission at 666 nm.

2.4 Cytotoxicity assays

Cytotoxicity of Y099 or Y099-Lip-Gel was assessed using the Cell Counting Kit-8 (CCK8) kit (#96992, Sigma, USA) as previously described [32]. Chondrocytes were seeded at a density of 5000–10,000 cells/well and cultured in 96-well plates for 24 h, followed by Y099 treatment for 24 h or Y099-Lip-Gel treatment for 24 h or 72 h. After the incubation with the CCK8 reagent, the absorbance value in the wavelength of 450 nm was detected using a microplate reader (BioTek, USA).

2.5 Chondrocytes isolation, culture, and drug treatment

Chondrocytes were obtained from the knee joints of 3-day-old C57BL/6 mice by sequential enzymatic digestion as previously described [33]. The animal tissue harvest was approved by the Experimental Animal Ethics Committee of Tongji Medical College, Huazhong University of Science and Technology (Wuhan, China) (IACUC: 2737). In brief, knee cartilage tissue was excised and immersed in PBS after the synovium, and other attachments were removed thoroughly from the cartilage tissue. Then, cartilage tissue was minced and digested with 0.25% trypsin for 30 min and 0.25% collagenase II (Invitrogen, USA) at 37 °C for 6 h sequentially. After the suspension was filtered by a 70-μm filter, chondrocytes were collected by centrifugation at 1500 r/min for 5 min and cultured in an incubator containing 5% CO_2 at 37 °C with DMEM/F12 medium supplemented with 10% FBS and 1% penicillin/streptomycin (#15140122, Gibco, USA). After cell passaging, chondrocytes of the second passage were used for experiments. Chondrocytes were induced by recombinant mouse IL-1β protein (5 ng/mL) for 24 h to obtain OA-like phenotypes. For the drug treatments, thermosensitive hydrogel loaded with Y099 was added to transwell inserts (Corning, USA) and solidified at 37 °C. After the chondrocytes reached 70–80% confluency, the pre-treated transwell inserts were plated into the cell culture wells with the insert bottoms immersed in the culture medium. The concentrations of Y099 were represented by the ratio of the total amount of Y099 to liquid volume.

2.6 Micromass culture

Micromass cultures were performed as previously described [34]. Briefly, passage 1st chondrocytes were plated at a density of 2.5×10^5 cells/10 μL drop on 24-well plates. The chondrocytes were treated with 5 ng/mL IL-1β and with or without

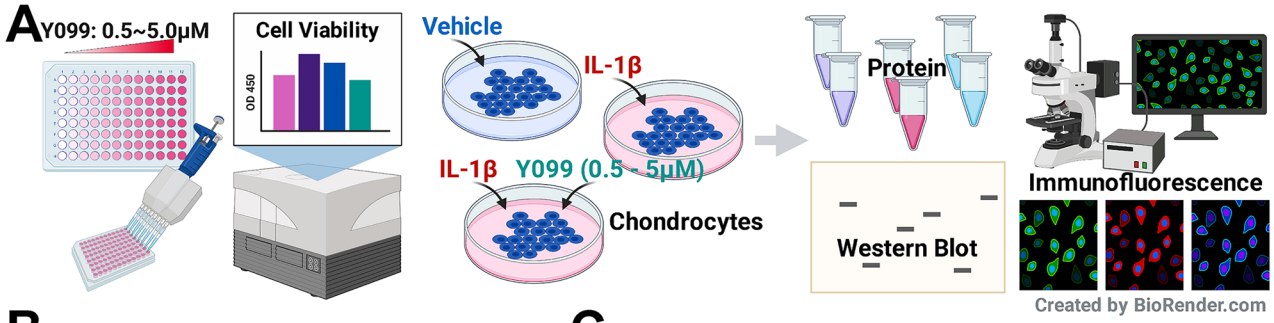
A
Y099: 0.5~5.0μM
Cell Viability
OD 450
Vehicle
IL-1β
IL-1β Y099 (0.5 ~ 5μM)
Chondrocytes
Protein
Western Blot
Immunofluorescence
Created by BioRender.com

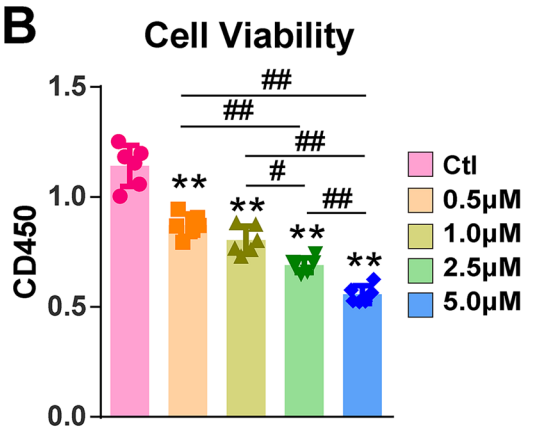
B
Cell Viability
CD450
Ctl
0.5μM
1.0μM
2.5μM
5.0μM

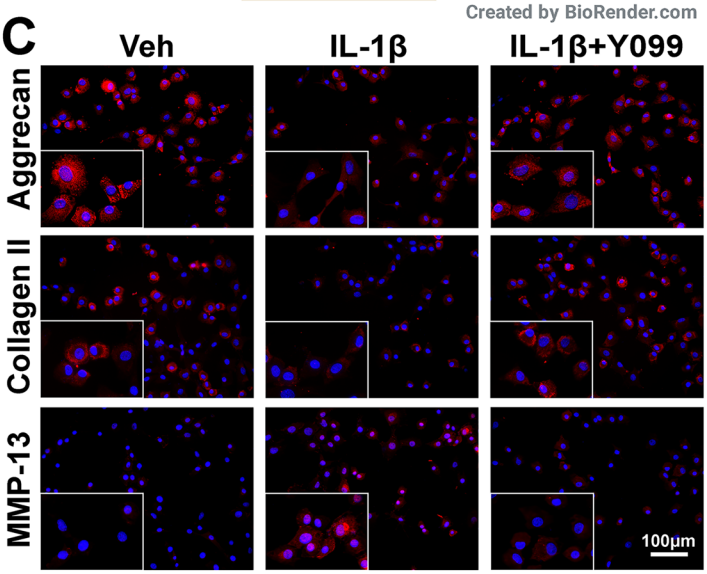
C
Veh
IL-1β
IL-1β+Y099
Aggrecan
Collagen II
MMP-13
100μm

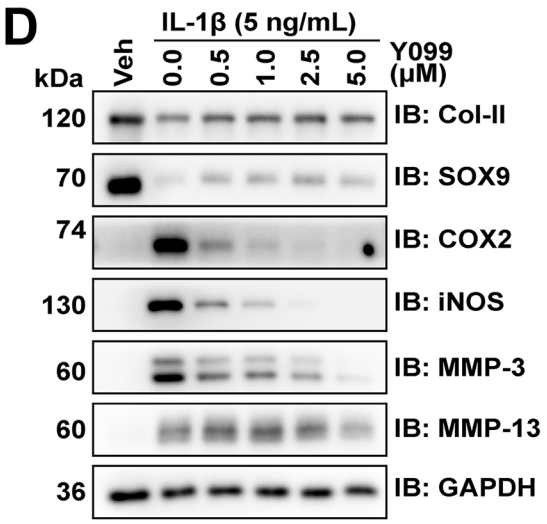
D
IL-1β (5 ng/mL)
kDa
Veh
Y099 (μM)
IB: Col-II
IB: SOX9
IB: COX2
IB: iNOS
IB: MMP-3
IB: MMP-13
IB: GAPDH

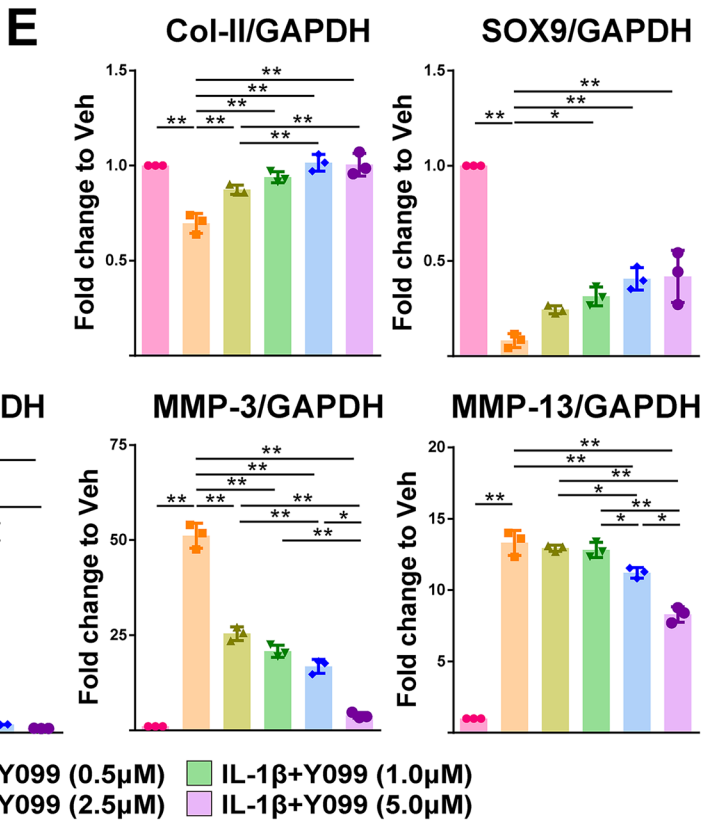
E
Col-II/GAPDH
SOX9/GAPDH
COX2/GAPDH
iNOS/GAPDH
MMP-3/GAPDH
MMP-13/GAPDH
Fold change to Veh
Veh
IL-1β
IL-1β+Y099 (0.5μM)
IL-1β+Y099 (1.0μM)
IL-1β+Y099 (2.5μM)
IL-1β+Y099 (5.0μM)

◂**Fig. 1** Kinase inhibitor Y099 suppresses the IL-1β-induced inflammation and catabolism and induces anabolism whereas causing the inhibition of cell viability. **A** Schematic diagram showing the treatments and experimental procedures of Y099. **B** Cell viability of the chondrocytes treated with Y099 for 24 h. Data represent mean ± SD; $N = 6$/group; $^{**}P < 0.01$ by one-way ANOVA, compared with the Ctl group; $^{\#}P < 0.05$, $^{\#\#}P < 0.01$ by one-way ANOVA. **C** Immunofluorescence staining of aggrecan, Type-II collagen, and MMP-13 in the vehicle-induced or IL-1β (5 ng/mL)-induced chondrocytes treated with or without 5.0 μM Y099 for 24 h. Scar bar: 400 μm. **D** Western blot analyses of the protein abundance of Type-II collagen, SOX9, COX, iNOS, MMP-3, MMP-13, and GAPDH in the vehicle-induced or IL-1β-induced chondrocytes treated with or without 5.0 μM Y099 for 24 h. (**D**) Quantitative analyses of western blots. Data represent mean ± SD; $N = 3$/group; $^{*}P < 0.05$; $^{**}P < 0.01$ by one-way ANOVA. Y099, YKL-05-099; Veh, vehicle; Col-II, Type-II collagen

Y099-Lip-Gel (Y099: 5 μM) for 72 h. Extracellular matrix proteoglycan contents were identified by Alcian blue staining.

2.7 RNA extraction, cDNA synthesis, and quantitative real-time PCR

Trizol reagent (#15596026, Invitrogen, USA) was used to extract RNA according to the manufacturer's instructions. Total RNA (1 μg) was used to synthesize cDNA using the HiScript II 1st Strand cDNA Synthesis Kit (#R211-01, Vazyme, China). mRNA levels of each gene of interest were normalized to *Gapdh* mRNA in the same sample, and the relative expression of the genes of interest was determined using the formula of Livak and Schmittgen [35]. The primers used for quantitative real-time PCR (qPCR) are listed in Table S1.

2.8 Western blot analysis

Protein extraction and western blot analysis were performed as the previous study described [36]. Briefly, total protein was extracted using radio-immunoprecipitation assay buffer according to the manufacturer's instructions. The total protein (10 μg) was resolved by sodium dodecyl-sulfate polyacrylamide gel electrophoresis and transferred to a polyvinylidene difluoride membrane. After being blocked with 5% bovine serum albumin, the membrane was incubated with the primary antibodies at 4 °C overnight and was rinsed thrice with tris-buffered saline with 0.1% Tween 20 for 15 min. The membrane was incubated with secondary antibodies for 1 h at room temperature and washed thrice with tris-buffered saline with 0.1% Tween 20 for 15 min. Protein blots were developed using a Western ECL substrate kit (#32106, Thermo Fisher Scientific, USA) and a Bio-Rad scanner (BioRad, USA). The intensity of bands was quantified by digital image analysis software (Bio-Rad, USA). Western blot analyses were performed in triplicate.

2.9 Immunofluorescence staining and β-galactosidase staining

Immunofluorescence (IF) staining was performed to check the effect of Y099 on chondrocytes. After being seeded at a density of 2×10^4 cells/dish and cultured for 24 h, chondrocytes were induced with IL-1β (5 ng/mL) and with or without Y099 (5 μM) for 24 h. After the fixation of 4% paraformaldehyde and the blockage of 1% bovine serum albumin, the chondrocytes were incubated with primary antibodies against aggrecan, Type-II collagen, and MMP-13 at 4 °C overnight. Chondrocytes were washed twice with PBS and incubated with secondary antibodies for 1 h at room temperature in the dark. The nuclei were dyed using 4',6-diamidino-2-phenylindole (DAPI) for 10 min. Fluorescence images were captured and scanned using a fluorescence microscope (Nikon, USA). To check whether Y099-Lip-Gel inhibits the DNA damage indicator γH2AX, chondrocytes were treated with or without IL-1β (5 ng/mL) and with or without Y099-Lip-Gel (Y099: 5 μM) for 24 h, and IF staining of γH2AX was performed using DNA damage detection kit (γ-H2AX immunofluorescence assay; #C2035S; Beyotime, China) according to the manufacturer's instructions. Fluorescence images of γH2AX were captured using a LEICA SP8 confocal laser scanning microscope (LEICA, German). To identify the senescent chondrocytes, β-galactosidase staining was performed using the senescence β-galactosidase staining kit (#9860; Cell Signaling Technology, USA) as previously described [37].

2.10 RNA sequencing analysis

Vehicle or IL-1β (5 ng/mL)-induced chondrocytes were treated with drug-free Lip-Gel or Y099-Lip-Gel (Y099: 5 μM) for 24 h; thus, four groups were involved (Ctl-Veh, Ctl-IL-1β, Y099-Veh, and Y099-IL-1β). Two biological replicates of each group were prepared for RNA sequencing (RNA-seq). Briefly, total RNA was isolated using Trizol, and qualified RNA (500 ng) was used to build cDNA libraries, which were sequenced using the Illumina HiSeq 4000 platform at Gene Denovo Biotechnology Co., Ltd (China). The sequencing data were processed as previously described [38]. Gene expression levels were indicated by FPKM (fragment per kilobase of transcript per million mapped reads). Principal component analysis (PCA) was used to determine the overall difference in transcriptome between each group. Differentially expressed genes (DEGs) were identified by the criteria of FDR < 0.05 using the R package *DESeq2* (v1.38.2) [39]. The perturbation amplitude of gene expression induced by the treatments was defined by expression variance calculated by the absolute value of the difference in normalized gene expression (FPKM) between the two groups to identify the robustly regulated genes. To identify

the commonly prioritized genes in the ranked list of up- or down-regulated genes induced by IL-1β and in the ranked list of the down- and up-regulated genes by Y099-Lip-Gel, which were ranked in descending order of expression variance values, normalized rescue score was defined using the R package *RobustRankAggreg* (v1.1) [40]. By comparing the perturbation amplitude induced by IL-1β or Y099-Lip-Gel, Type-1 and Type-2 rescued genes were defined. Type-1 genes were defined as the completely rescued ones, whose perturbation amplitudes induced by Y099-Lip-Gel were greater than the ones induced by IL-1β. Type-2 genes were the partially rescued ones whose perturbation amplitudes induced by Y099-Lip-Gel were smaller than the ones induced by IL-1β. Gene ontology (GO) and Kyoto Encyclopedia of Genes and Genomes (KEGG) enrichment analyses and gene set enrichment analysis (GSEA) were performed using the R package *clusterProfiler* (v3.11) [41]. Senescence-related gene sets were sourced from CellAge (Build 2) [42]. For GSEA, FDR < 0.25 was considered significant.

2.11 Phosphoproteomic analysis

Chondrocytes were prepared and treated as they were done in the RNA-seq study. Two biological replicates of each group were prepared for phosphoproteomic analysis. After the drug treatment, chondrocyte pallets were collected. Subsequent protein sample preparation and liquid chromatography-tandem mass spectrometry (LC–MS/MS) were performed at Jingjie PTM Biolab Co., Ltd. (China). Briefly, the protein of chondrocyte pallets was extracted, and the protein samples underwent trypsin digestion to generate peptide mixtures which were further labeled with tandem mass tag (TMT) (ThermoFisher Scientific, USA) according to the manufacturer's instructions. The TMT-labeled peptides were fractionated by high pH reverse-phase HPLC using Agilent 300 Extend C18 column (5 μm particles, 4.6 mm ID, 250 mm length). Then, the phosphopeptides of each fraction were enriched with immobilized metal affinity chromatography (IMAC)-TiQ2 and analyzed using LC–MS/MS. Data were processed using the MaxQuant search engine (v.1.5.2.8) and analyzed using bioinformatics methods [43, 44]. Phosphosites with a ratio of estimated phosphorylation levels > 1.3 or < 1/1.3 and a coefficient of variation (CV) < 0.1 were considered significant [45]. Kinome tree was visualized using Coral [46]. KEGG enrichment analysis and GSEA of the significant phosphosites were performed using the R package *clusterProfiler* (v3.11) [41]. For GSEA, FDR < 0.25 was considered significant.

2.12 Animal study

All the protocols of animal study were approved by the Experimental Animal Ethics Committee of Tongji Medical College, Huazhong University of Science and Technology (Wuhan, China) (IACUC: 2737). Sixty 8-week-old male C57BL/6 J mice were purchased from Wuhan Beiente Biology Science and Technology Co., Ltd. and fed in a specific-pathogen-free animal environment. The OA model was established by the surgical destabilization of the medial meniscus (DMM) after inhalation-induced anesthesia with isoflurane. The sham animals were subjected to the surgical incision of the joint cavity and excision of the anterior fat pad. The mice were randomly and evenly assigned into five groups, including (1) sham; (2) DMM; (3) DMM treated with the hydrogel loaded with drug-free nanoliposomes (Lip-Gel) (DMM-0 mg/mL); (4) DMM treated with Y099-Lip-Gel loaded with 1.5 mg/mL Y099 (DMM-1.5 mg/mL); and (5) DMM treated with Y099-Lip-Gel loaded with 3.0 mg/mL Y099 (DMM-3.0 mg/mL). One-week post-surgery, the mice were treated with the first intra-articular injections of 10 μL drugs and subsequently treated every 2 weeks for 6 weeks. The mice of the sham or DMM group received 10 μL saline solution. The mice were sacrificed, and the right knee joints were collected for analysis after all the injections were finished. The major organs, including the heart, liver, spleen, kidney, and testis, were fixed by 4% PFA and subjected to hematoxylin and eosin (H&E) staining following standard protocol.

2.13 Microcomputed tomography analysis

After the fixation in 4% paraformaldehyde, microcomputed tomography (μCT) analysis of the joint was conducted using Scanco vivaCT 40 (Scanco Medical, Switzerland) with the following parameters of calcified tissue visualization: voxel size of 10 μm resolution, voltage of 100 kV, current of 98 μA, and integration time of 300 ms. The 3D reconstructed images and quantitative analysis data were generated by 3D built-in software. The parameters of the tibial subchondral bone, including trabecular bone volume (BV)/tissue volume (TV) fraction (BV/TV), trabecular thickness (Tb. Th), trabecular spacing (Tb. Sp), and trabecular number (Tb. N), were measured as previously described [47]. The surface roughness analysis was performed in the medial femoral condyle using ImageJ software v1.53 k (National Institutes of Health, USA).

2.14 Histomorphometric and immunohistochemistry analyses

The knee joints were decalcified in 10% ethylenediaminetetraacetic acid (EDTA) for 30 days after the fixation in 4% paraformaldehyde at 4 °C, subsequentially embedded in paraffin, and sliced into 5-μm sections. Safranin O (Saf-O)/fast green staining was performed for histological assessment of

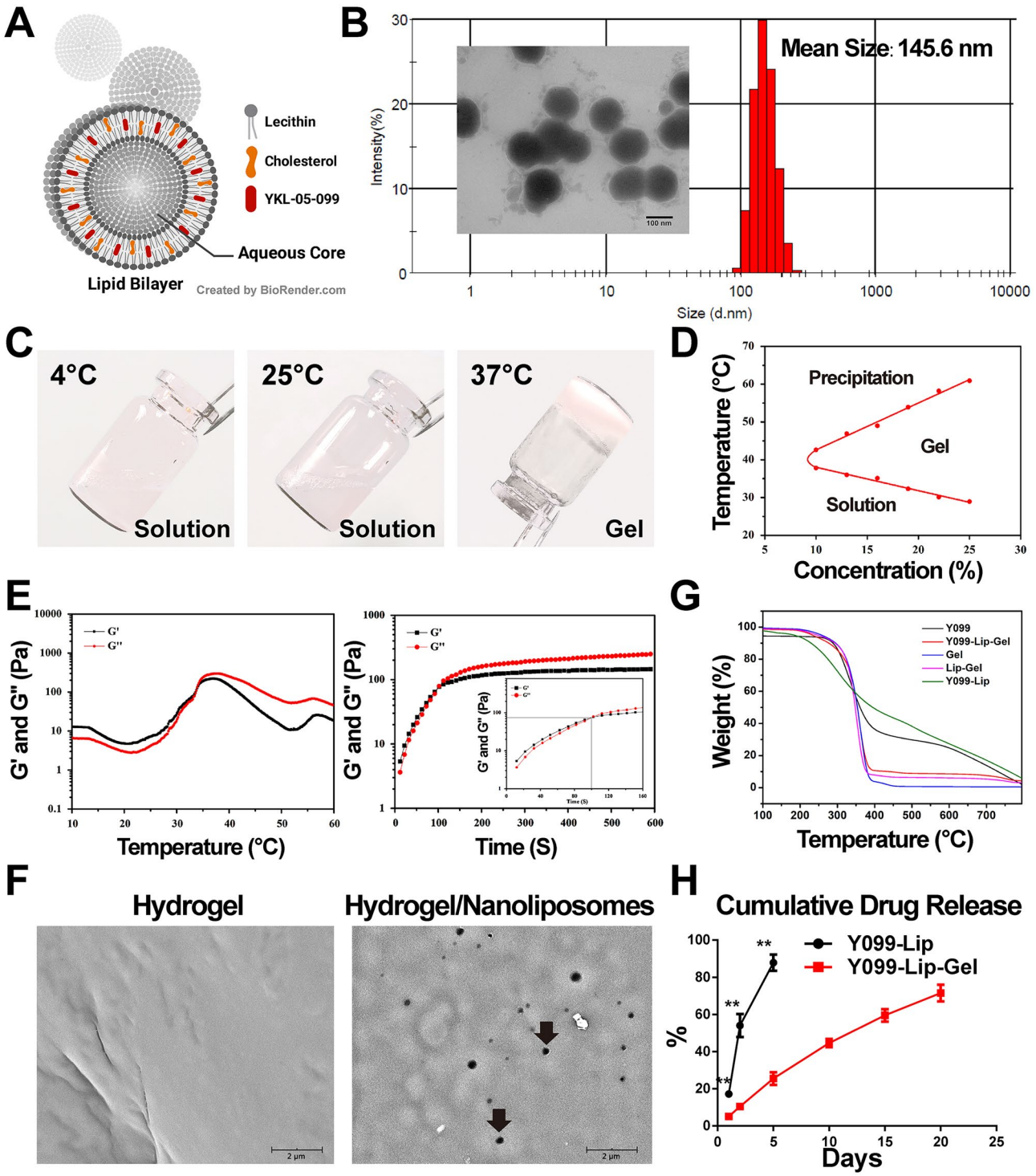

Fig. 2 Characterization of Y099-Lip-Gel. **A** Structural schematic diagram of Y099-loaded nanoliposome. **B** Representative images of transmission electron microscopy and diameter measurement of Y099-loaded nanoliposomes. Scar bar: 100 μm. **C** Images of the polymer at 4 °C, 25 °C, and 37° C. **D** Solution-gel phase transition diagram of the polymer. **E** Temperature and time dependence of storage (*G*') and loss modulus (*G*") of the polymer aqueous solution (25 wt%). The maximum temperature of modulus was 33.8 °C (left) and the gelation time was 99.2 s at 37 °C (right). **F** Images of scanning electron microscope showing the distribution of Y099-loaded nanoliposomes in the hydrogel. Y099-loaded nanoliposomes are indicated by black arrows. The white spots are the hydrogel lumps formed during lyophilization. **G** Thermogravimetric analysis showing that the hydrogel promoted the thermal stability of Y099-loaded nanoliposomes. **H** Drug release curve of Y099-Lip-Gel in vitro. Data represent mean ± SD; $N = 3$/group; $^{**}P < 0.01$ by Student's *t*-test, Y099-Lip versus Y099-Lip-Gel

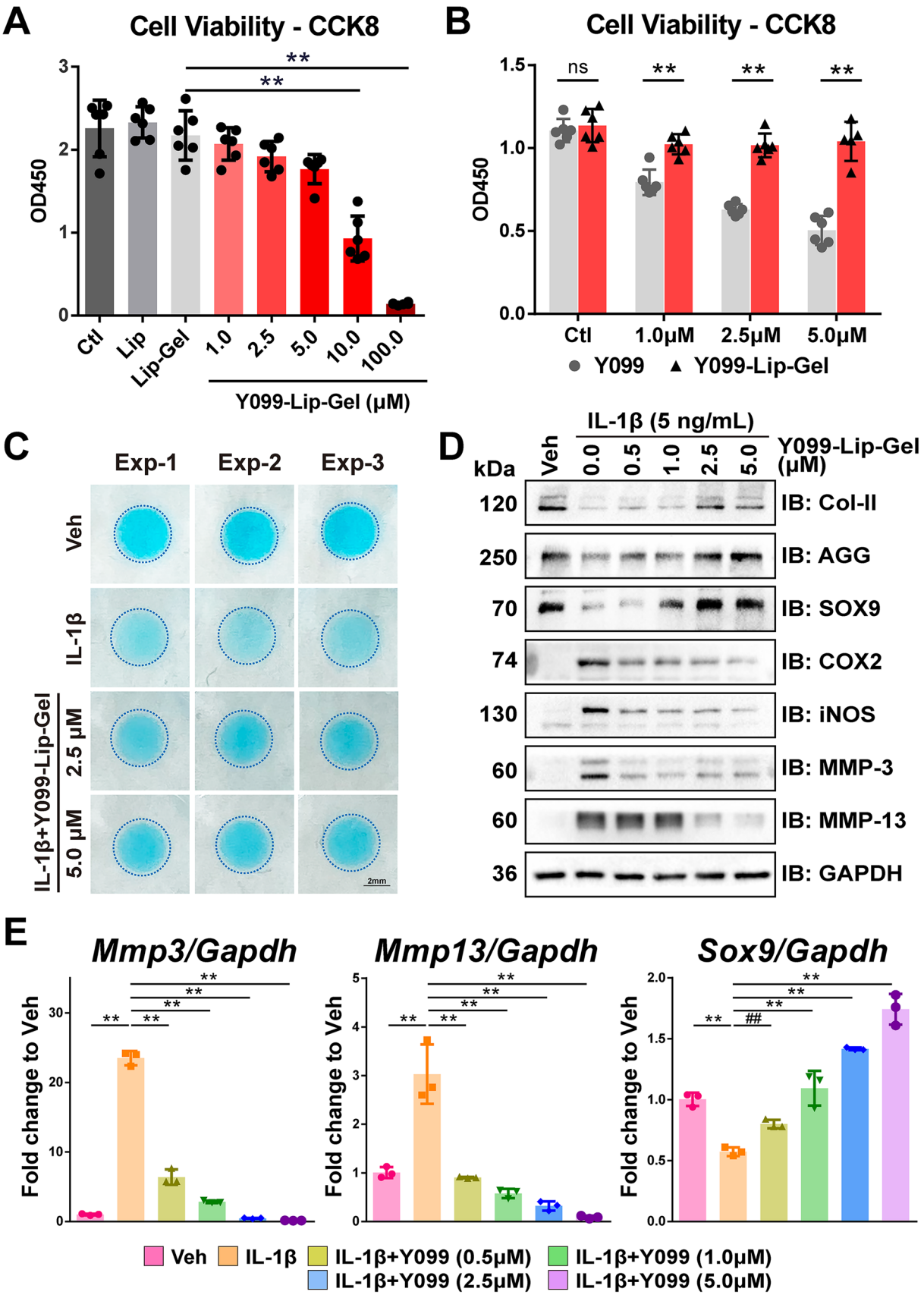
A
Cell Viability - CCK8
OD450
Ctl
Lip
Lip-Gel
1.0
2.5
5.0
10.0
100.0
Y099-Lip-Gel (μM)
B
Cell Viability - CCK8
OD450
ns
Ctl
1.0μM
2.5μM
5.0μM
Y099
Y099-Lip-Gel
C
Exp-1
Exp-2
Exp-3
Veh
IL-1β
IL-1β+Y099-Lip-Gel
2.5 μM
5.0 μM
2mm
D
IL-1β (5 ng/mL)
Veh
Y099-Lip-Gel (μM)
kDa
120
IB: Col-II
250
IB: AGG
70
IB: SOX9
74
IB: COX2
130
IB: iNOS
60
IB: MMP-3
60
IB: MMP-13
36
IB: GAPDH
E
Mmp3/Gapdh
Mmp13/Gapdh
Sox9/Gapdh
Fold change to Veh
Veh
IL-1β
IL-1β+Y099 (0.5μM)
IL-1β+Y099 (1.0μM)
IL-1β+Y099 (2.5μM)
IL-1β+Y099 (5.0μM)

◂**Fig. 3** Y099-Lip-Gel exhibits a pronounced effect on promoting anabolism and suppressing catabolism and inflammation without causing the inhibition of chondrocyte viability. **A** Cell viability of the chondrocytes treated with Y099-Lip-Gel for 72 h. Data represent mean ± SD; $N = 6$/group; $^{**}P < 0.01$ by one-way ANOVA. **B** Cell viability of the chondrocytes treated with Y099 or Y099-Lip-Gel at the same concentration for 24 h. Data represent mean ± SD; $N = 6$/group; $^{**}P < 0.01$ by Student's *t*-test; ns, not significant. **C** Images of Alcian blue staining showing the IL-1β (5 ng/mL)-induced chondrocyte micromass treated with Y099-Lip-Gel for 72 h. Scar bar: 2 mm. **D** Western blot analyses of the protein abundance of Type-II collagen, aggrecan, SOX9, COX, iNOS, MMP-3, and MMP-13, and GAPDH in the vehicle-induced or IL-1β-induced chondrocytes treated with or without Y099-Lip-Gel for 24 h. **E** qPCR analyses of the mRNA levels of *Mmp3*, *Mmp13*, and *Sox9* in the vehicle-induced or IL-1β-induced chondrocytes treated with or without Y099-Lip-Gel for 24 h. Y099, YKL-05-099; Y099-Lip, nanoliposomal Y099; Y099-Lip-Gel, hydrogel loaded with nanoliposomal Y099; Veh, vehicle; Col-II, Type-II collagen; AGG, aggrecan

cartilage to observe chondrocyte morphology and arrangement, articular cartilage structure, and extracellular matrix abundance. The OA Research Society International (OARSI) scoring system (0 to 6) and modified Mankin scoring system (0 to 16) were used to semi-quantitatively analyze cartilage lesions [48, 49]. Saf-O abundance reflecting proteoglycan content was scored (0 to 12) according to the previous studies [47, 50]. The mean value of three individual scores assessed by three blinded researchers was calculated for one slide, and the mean score of randomly chosen ten slides was calculated to represent one sample. A higher score indicates more advanced histological lesions of OA. Tartrate-resistant acid phosphatase (TRAP) staining was performed to analyze the osteoclast number in the femoral condyle as previously described [51]. Immunohistochemistry (IHC) analyses of the joints and human cartilage explants were performed as previously described [52].

2.15 Human cartilage harvest, culture, and treatment

Human tissue harvest was approved by the Human Ethics Committee of Tongji Medical College, Huazhong University of Science and Technology (Wuhan, China) (approval number: TJ-IRB20220946). Six OA patients (mean age, 67 years; range, 59–72 years; male: 4, female: 2) who underwent total knee arthroplasty (TKA) at the Department of Orthopedics, Tongji Hospital, Tongji Medical College, Huazhong University of Science and Technology, in 2022 were enrolled in this study. None of them had other systemic diseases. Written informed consent was acquired from each patient before the sample was obtained. The medial femoral condyles were isolated from the OA patients during surgery and quickly transformed to the laboratory on ice for further processing. The medial femoral condyles were washed three times using PBS and further immersed in PBS, followed by the removal of the soft tissue clearance on the cartilage surface. The cartilage explants sized in $5 \times 5 \times 5$ mm^3 were excised using a surgical saw and immersed in PBS for later treatment. The cartilage explants were cultured in an incubator containing 5% CO_2 at 37 °C with DMEM/F12 medium supplemented with 10% FBS, 1% penicillin/streptomycin, and human IL-1β (10 ng/mL). For drug treatment, the cartilage explants from the same patient were treated drug-free Lip-Gel or Y099-Lip-Gel (Y099: 5 μM) for 48 h. Briefly, the transwell inserts added with solidified Y099-Lip-Gel (Y099: 5 μM) were plated into the cell culture wells with the insert bottoms immersed in the culture medium. After 48-h treatment, the cartilage explants were fixed in 4% paraformaldehyde at 4 °C for 24 h and decalcified in 10% EDTA for 30 days, followed by the standard procedures of IHC analysis.

2.16 Statistical analysis

All data analyses were conducted using GraphPad Prism software v7.0 (GraphPad, USA). Comparisons between the two groups were performed by unpaired *t*-test. Comparisons among multiple groups were performed by one-way analysis of variance (ANOVA) followed by Tukey's test. A p value < 0.05 was recognized as significant. All the experiments were repeated three times, and independently triplicate data were displayed as means and standard deviations.

3 Results

3.1 Y099 notably suppresses inflammation and catabolism and promotes anabolism in IL-1β-treated chondrocytes while causing viability inhibition

The cytotoxicity of Y099 was first checked by the CCK8 method (Fig. 1A and B). After 24-h treatment, the cell viability of chondrocytes was notably suppressed by Y099 (0.5–5 μM) in a dose-dependent manner (~20% decreased at 1.0 μM; ~50% at 5.0 μM) (Fig. 1B). To assess whether Y099 affects the anabolism and catabolism of IL-1β-treated chondrocytes, the expression of cartilage anabolic indicators aggrecan and Type-II collagen and catabolic indicator MMP-13 was detected by IF analyses (Fig. 1C). IL-1β (5 ng/mL) suppressed the abundance of aggrecan and Type-II collagen and induced the expression of MMP-13, whereas Y099 (5.0 μM) rescued the effects of IL-1β by increasing aggrecan and Type-II collagen and inhibiting MMP-13 after 24-h treatment. These findings were validated by western blot (Fig. 1D and E). The western blot showed that MMP-3, a catabolic indicator like MMP-13, was more sensitive to

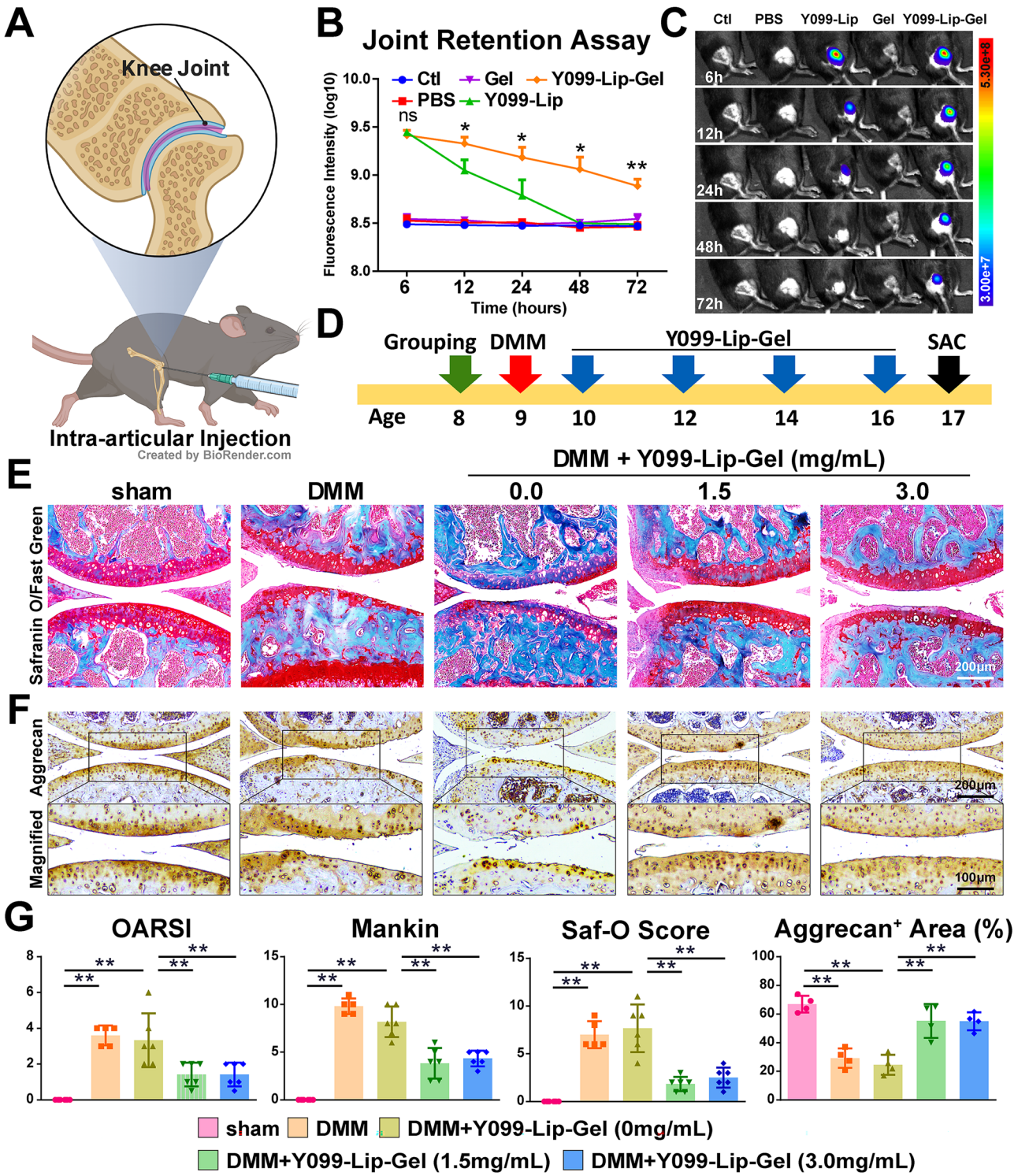

Fig. 4 Y099-Lip-Gel attenuates the histological cartilage lesions and promotes aggrecan synthesis in the OA murine model. **A** Schematic diagram of intra-articular injection in the knee joint. **B** Quantitative analyses of joint retention assay by in vivo fluorescence method. 10 μL of hydrogel with Cy5-loaded nanoliposomal Y099 or 10 μL of Cy5-loaded nanoliposomal Y099 was injected into the knee joint of the 12-week-old C57 mice. Data represent mean ± SD; N = 3/group. $^{**}P < 0.05$, $^{**}P < 0.01$ by Student's *t*-test, Y099-Lip-Gel versus Y099-Lip. **C** Representative images of Cy5 fluorescence showing the joint retention of injections. **D** Injection protocol of the Y099-Lip-Gel treatment in the OA murine model. The OA model was established by the surgical destabilization of the medial meniscus (DMM). **E** Safranin O-fast green staining showing knee sagittal sections. Scar bar: 200 μm. **F** Immunohistochemistry representative images of the aggrecan protein abundance. **G** Statistical analysis of OARSI histological scores, Mankin scores, Saf-O scores, and aggrecan positive area percentages. Data represent mean ± SD; $N = 6$/group; $^{**}P < 0.01$ by one-way ANOVA

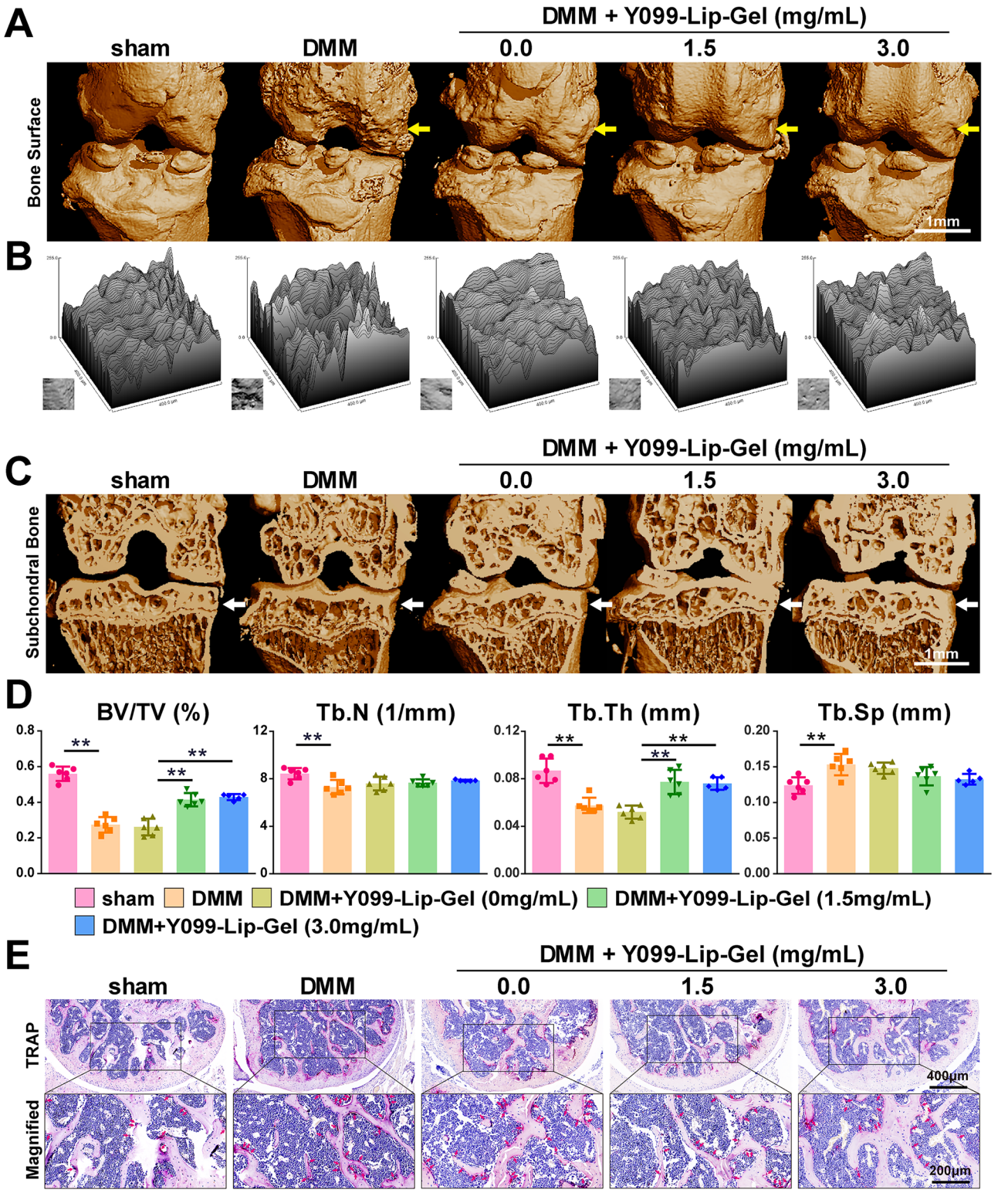

Fig. 5 Y099-Lip-Gel inhibits osteophyte formation, subchondral bone loss, and osteoclast formation in the OA murine model. **A** μCT representative 3D images showing the bone surface of the femoral condyle and tibial plateau. Yellow arrows indicate the osteophyte formations on the surface. Scar bar: 1 mm. **B** Surface roughness analyses of the medial femoral condyle. **C** μCT representative 3D images showing the coronal section of femurs and tibias. White arrows indicate the subchondral bone of the tibia. Scar bar: 1 mm. **D** Quantitative analysis of the parameters of tibial subchondral bone including trabecular bone volume (BV)/tissue volume (TV) fraction (BV/TV), trabecular number (Tb. N), trabecular thickness (Tb. Th), and trabecular separation (Tb. Sp). Data represent mean ± SD; $N = 6$/group; $^{**}P < 0.01$ by one-way ANOVA. **E** Tartrate-resistant acid phosphatase (TRAP) staining showing the osteoclasts in the femoral condyle

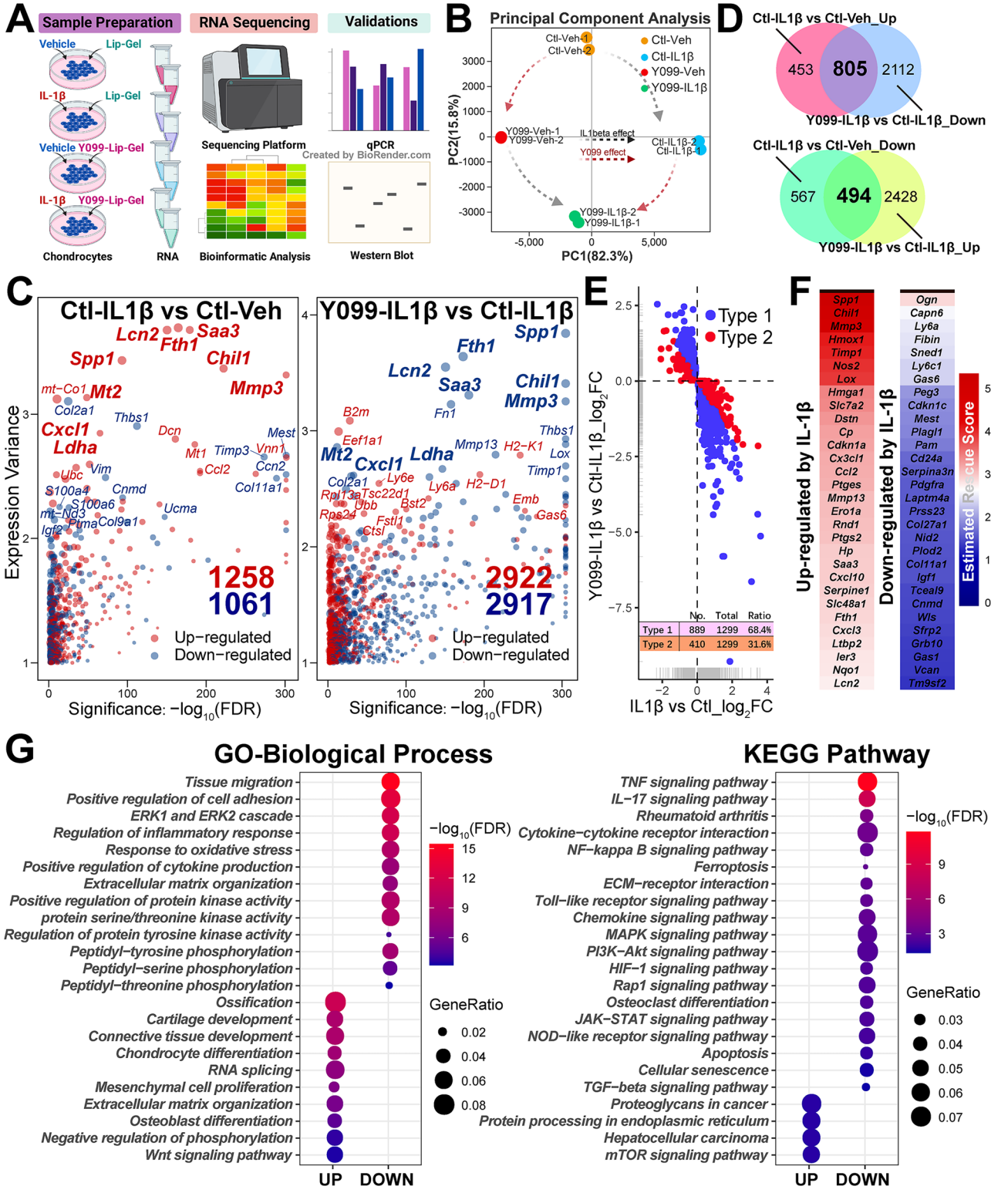

the Y099 treatment, which was ~ 50% decreased by Y099 (0.5 μM) and almost completely inhibited by Y099 (5.0 μM). In line with the changes of aggrecan and Type-II collagen, SOX9, the master regulator of chondrocyte phenotypes, was also moderately increased by the Y099 treatment. Furthermore, the expression of inflammation indicators COX and iNOS were notably enhanced by IL-1β, whereas Y099 showed a pronounced inhibition in COX and iNOS even at a low concentration (0.5 μM) (Fig. 1D and E). These findings demonstrated that Y099 has a remarkable suppressive effect

◂**Fig. 6** Y099-Lip-Gel recuses IL-1β-induced gene expression and regulates OA-related signaling pathways. **A** Schematic diagram of the RNA sequencing (RNA-seq) study design. The vehicle-induced or IL-1β-induced chondrocytes treated with or without Y099-Lip-Gel (Y099: 5 μM) for 24 h were subjected to RNA-seq analysis. **B** Principal component analysis showing the effects of IL-1β or Y099-Lip-Gel on the overall transcriptome. The transcriptomic difference was mainly defined by the distance in the PC1 axis. Ctl-Veh: the vehicle-induced chondrocytes treated with drug-free Lip-Gel; Ctl-IL-1β: the IL-1β (5 ng/mL)-induced chondrocytes treated with drug-free Lip-Gel; Y099-Veh: the vehicle-induced chondrocytes treated with Y099-Lip-Gel (Y099: 5 μM); Y099-IL-1β: the IL-1β (5 ng/mL)-induced chondrocytes treated with Y099-Lip-Gel (Y099: 5 μM). **C** Scatter plots of the differentially expressed genes (DEGs) in the comparison between Ctl-IL-1β and Ctl-Veh or between Y099- IL-1β and IL-1β. The up- or down-regulated DEGs are indicated in red or blue color. The top 15 up- or down-regulated DEGs in the ranked gene list sorted in descending order of expression variance values are labeled by official gene symbols. The rescued genes, including *Mmp3*, *Chil1*, *Saa3*, *Fth1*, *Lcn2*, *Spp1*, *Mt2*, *Cxcl1*, and *Ldha* are labeled in bold. Expression variance is defined by the absolute value of the difference in normalized gene expression (FPKM). **D** Venn plots of the DEGs showing the common genes with an opposite response to IL-1β or Y099-Lip-Gel. **E** The scatter plot of the completely-rescued (Type-1) and partially-rescued (Type-2) genes defined by perturbation amplitudes. **F** Top 30 IL-1β-induced or suppressed genes remarkably rescued by Y099-Lip-Gel. **G** Gene ontology (GO) and Kyoto Encyclopedia of Genes and Genomes (KEGG) enrichment analyses of the rescued genes ($n=1299$). GeneRatio indicates the gene number ratio in each GO or KEGG item. The color and size of the dot represent the p value adjusted by Benjamini and Hochberg method (FDR) and the gene number assigned to the corresponding GO or KEGG item, respectively. UP: the up-regulated genes by Y099-Lip-Gel that were suppressed by IL-1β; DOWN: the down-regulated genes by Y099-Lip-Gel that were increased by IL-1β

on inflammation and catabolism and a moderate promotion of anabolism while causing considerable viability inhibition.

3.2 Y099-Lip-Gel remains beneficial effects of Y099 on chondrocytes, enhancing the promotion of Sox9 expression without causing viability inhibition

To overcome the limitation of Y099 in cytotoxicity, Y099-Lip-Gel was developed for sustained release and toxicity exemption. As shown in Fig. 2A, Y099 is loaded in the lipid bilayer of nanoliposomes. The Y099-loaded nanoliposomes with a mean particle size of 145.6 nm were evenly dispersed (Fig. 2B). The PLGA1500-PEG1200-PLGA1500 polymers (25 wt%) displayed temperature-dependent solution-gel transition behavior, which exhibited solution-like behavior at 4 °C and room temperature (25 °C) and formed a gel at body temperature (37 °C) (Fig. 2C and D). The modulus-temperature cure showed that the maximum temperature of the modulus of the polymer solution (25 wt%) was 33.8 °C (Fig. 2E). The modulus-time cure demonstrated that the gelation time was 99.2 s at 37 °C (Fig. 2E), which is appreciated for performing the intra-articular injections of this gel-forming polymer solution and for the retention in the joint by gelation. SEM showed that the Y099-loaded nanoliposomes were evenly dispersed in the hydrogel (Fig. 2F). Thermogravimetric analysis showed that the hydrogel promoted the thermal stability of Y099-loaded nanoliposomes (Fig. 2G). Moreover, the drug release assay showed that more than 80% of Y099 was released from the nanoliposome in 5 days, whereas the hydrogel prolonged the drug release and more than 30% drug could be retained on the 20th day (Fig. 2F).

To determine whether the sustained release of Y099 could reduce cytotoxicity, the viability of the chondrocytes treated with Y099-Lip-Gel loaded with 1.0, 2.5, 5.0, 10.0, or 100.0 μM Y099 for 72 h was assessed by the CCK8 method. As shown in Fig. 3A, nanoliposomes or hydrogel themselves show no cytotoxicity, and Y099-Lip-Gel shows good cytocompatibility at the concentration from 1.0 to 5.0 μM. Of note, Y099-Lip-Gel (5.0 μM) showed considerable strength in toxicity exemption when compared with Y099 at 5.0 μM (Fig. 3B). To investigate whether Y099-Lip-Gel remained the beneficial effects of Y099 on chondrocytes, Alcian blue staining of micromass was performed to check the matrix abundance under the treatment of Y099-Lip-Gel. As shown in Fig. 3C, IL-1β reduces the matrix abundance of micromass, whereas Y099-Lip-Gel rescues this reduction caused by IL-1β. Western blot analyses showed that Y099-Lip-Gel remained the suppressive effects on the IL-1β-induced catabolic and inflammatory indicators (Fig. 3D). Although the suppressions of COX and iNOS were attenuated due to sustained release, the effects on promoting SOX9 and inhibiting MMP-13 were enhanced (Fig. 3D). These findings of MMP-3, MMP-13, and SOX9 were further validated by qPCR, which showed that Y099 regulated the expression of these indicators at the transcriptional levels (Fig. 3E). Of note, both western blot and qPCR showed that Y099-Lip-Gel exhibited an enhanced promotive effect on *Sox9* expression which is critical for cartilage homeostasis and OA development, suggesting a notable potential of Y099-Lip-Gel in OA therapy. These findings together indicated that sustained release of Y099 achieved by thermosensitive hydrogel loaded with nanoliposomes succeeded in toxicity exemption and reached a good balance on anabolism promotion and catabolism inhibition.

3.3 Y099-Lip-Gel attenuates histological cartilage lesions and subchondral bone loss in the OA murine model

To check whether hydrogel prolongs the retention of nanoliposomes in the joint, 10 μL PBS, Cy5-labeled nanoliposomes, hydrogel, or hydrogel loaded with Cy5-labeled nanoliposomes were administrated by intra-articular injections (Fig. 4A). The Cy5 fluorescence was dismissed 48 h after the injection of Cy5-labeled liposomes, whereas the hydrogel preserved the fluorescence for 72 h (Fig. 4B and

C). To evaluate the potential of Y099-Lip-Gel in OA therapy, the murine OA model was established by DMM surgery and received four injections of Y099-Lip-Gel by intra-articular administration for 2 months (Fig. 4D). H&E staining showed that Y099-Lip-Gel did not induce appreciable histological changes in the key organ after the 2-month treatment (Supplemental Fig. 1). The Saf-O/fast green staining of articular cartilage showed that DMM surgery induced typical OA-like cartilage degeneration, characterized by matrix loss, disorganized chondrocyte sequence, and fissures, whereas these changes were attenuated by Y099-Lip-Gel (Fig. 4E). The histological lesions of cartilage were further quantitatively analyzed by OARSI and modified Mankin scoring system. As shown in Fig. 4G, the DMM and DMM-0 mg/mL groups both show a considerable increase in OARSI and Mankin scores. However, both treatment groups showed lower scores than the DMM or DMM-0 mg/mL groups (Fig. 4G). Moreover, Saf-O scoring was used as a supplementary assessment of matrix loss, which showed that Y099-Lip-Gel partially rescued the elevation of the Saf-O score induced by DMM (Fig. 4G). To further assess the anabolic effect of Y099-Lip-Gel, IHC analyses of aggrecan were performed. The results showed that Y099-Lip-Gel attenuated the loss of aggrecan induced by DMM (Fig. 4F), which is consistent with the quantitative analyses of aggrecan positive area (Fig. 4G). These findings suggested that Y099-Lip-Gel attenuated histological cartilage lesions and promoted aggrecan synthesis against trauma-induced OA.

Osteophyte or bone spur formation is characterized in OA patients and experimental models, causing OA-related chronic pain. The 3D images of the joints developed by μCT analysis demonstrated that the obvious osteophytes were formed on the femoral surface of the DMM group, whereas osteophyte formation was ameliorated by Y099-Lip-Gel (Fig. 5A). The surface roughness analyses of the medial femoral condyle showed that the roughness was notably increased in the DMM group, whereas Y099-Lip-Gel attenuated the increased roughness of bone surface induced by DMM (Fig. 5B). Since subchondral bone is a critical element of the osteochondral unit in maintaining cartilage homeostasis, the bone mass and microstructure of tibial subchondral bone were analyzed by μCT (Fig. 5C). The coronal section of femurs and tibias showed that subchondral bone was reduced in the DMM group compared with the sham group, whereas Y099-Lip-Gel efficiently prevented the subchondral bone loss induced by DMM (Fig. 5D). The quantitative analyses of tibias showed that Y099-Lip-Gel exhibited an efficient action in increasing Tb. Th, thus leading to an increased BT/TV (Fig. 5D). Since osteoclast is an essential regulator of subchondral bone remodeling, subchondral osteoclast numbers were analyzed by TRAP staining. As shown in Fig. 5E and Supplemental Fig. 2, the osteoclast number is increased in the DMM group whereas decreased in the Y099-Lip-Gel groups. These findings indicated that Y099-Lip-Gel inhibited the OA-related osteophyte formation, subchondral bone loss, and osteoclast formation in the OA murine model.

3.4 Y099-Lip-Gel recuses IL-1β-induced gene expression and regulates OA-related signaling pathways

To decipher the mechanism by which Y099-Lip-Gel is against OA, transcriptomic analyses by RNA-seq were performed (Fig. 6A). The PCA result indicated the overall transcriptomic similarity and differences of samples (Fig. 6B). As shown in Fig. 6B, IL-1β induced a transcriptomic shift in the PC1 axis, which was opposed to the effect of Y099-Lip-Gel on the transcriptomic shift in the PC1 axis. Compared with the Ctl-Veh group, 2319 DEGs were identified in the Ctl-IL-1β group, including 1258 up-regulated and 1061 down-regulated genes (Fig. 6C). However, compared with the Ctl-IL-1β group, 2922 up-regulated and 2917 down-regulated genes were identified in the Y099-IL-1β group (Fig. 6C). Of note, *Mmp3*, *Chil1*, *Saa3*, *Fth1*, *Lcn2*, *Spp1*, *Mt2*, *Cxcl1*, and *Ldha* were notably up-regulated by IL-1β, whereas they were remarkably down-regulated by Y099-Lip-Gel (Fig. 6C). Indeed, ~ 69.4% of up-regulated genes ($n = 805$) and ~ 46.6% of down-regulated genes ($n = 494$) induced by IL-1β were rescued by Y099-Lip-Gel (Fig. 6D). Moreover, two types of rescued genes were further characterized by comparing the perturbation amplitudes of gene expression (Fig. 6E). The Type-1 genes ($n = 889$; 68.4%) were defined as completely rescued genes since the perturbation amplitudes induced by Y099-Lip-Gel were greater than the ones induced by IL-1β. The Type-2 genes ($n = 410$; 31.6%) were defined as partially rescued genes, which were much less than the Type-1 genes (Fig. 6E). To identify the most significantly rescued genes, a robust rank aggregation algorithm was employed to define a normalized rescued score which was to identify the common polarized gene in the comparisons between the Ctl-IL-1β and Ctl-Veh groups or between the Y099-IL-1β and Ctl-IL-1β groups and reflected the rescuing efficacy of Y099-Lip-Gel to IL-1β treatment at gene levels. According to the normalized rescued scores, the top 30 rescued genes are shown in Fig. 6F. In addition to catabolic genes such as *Mmp3* and *Mmp13*, inflammation-related genes (e.g., *Nos2*, *Cx3cl1*, *Ccl2*, *Cxcl3*, and *Cxcl10*) and tissue remodeling-related genes (e.g., *Spp1*, *Timp1*, and *Ogn*) were also identified in the top rescued gene list. Of note, *Cdkn1a*, which encodes cyclin-dependent kinase inhibitor 1A ($P21^{Cip1}$) and is a critical regulator and indicator of cellular senescence, was remarkably induced by IL-1β but suppressed by Y099-Lip-Gel. To understand the pathways related to these recused genes, these genes were subjected to GO and KEGG enrichment analyses (Fig. 6G). The pathways related to tissue remodeling and homeostasis pathways (e.g., tissue migration, ECM organization), inflammation

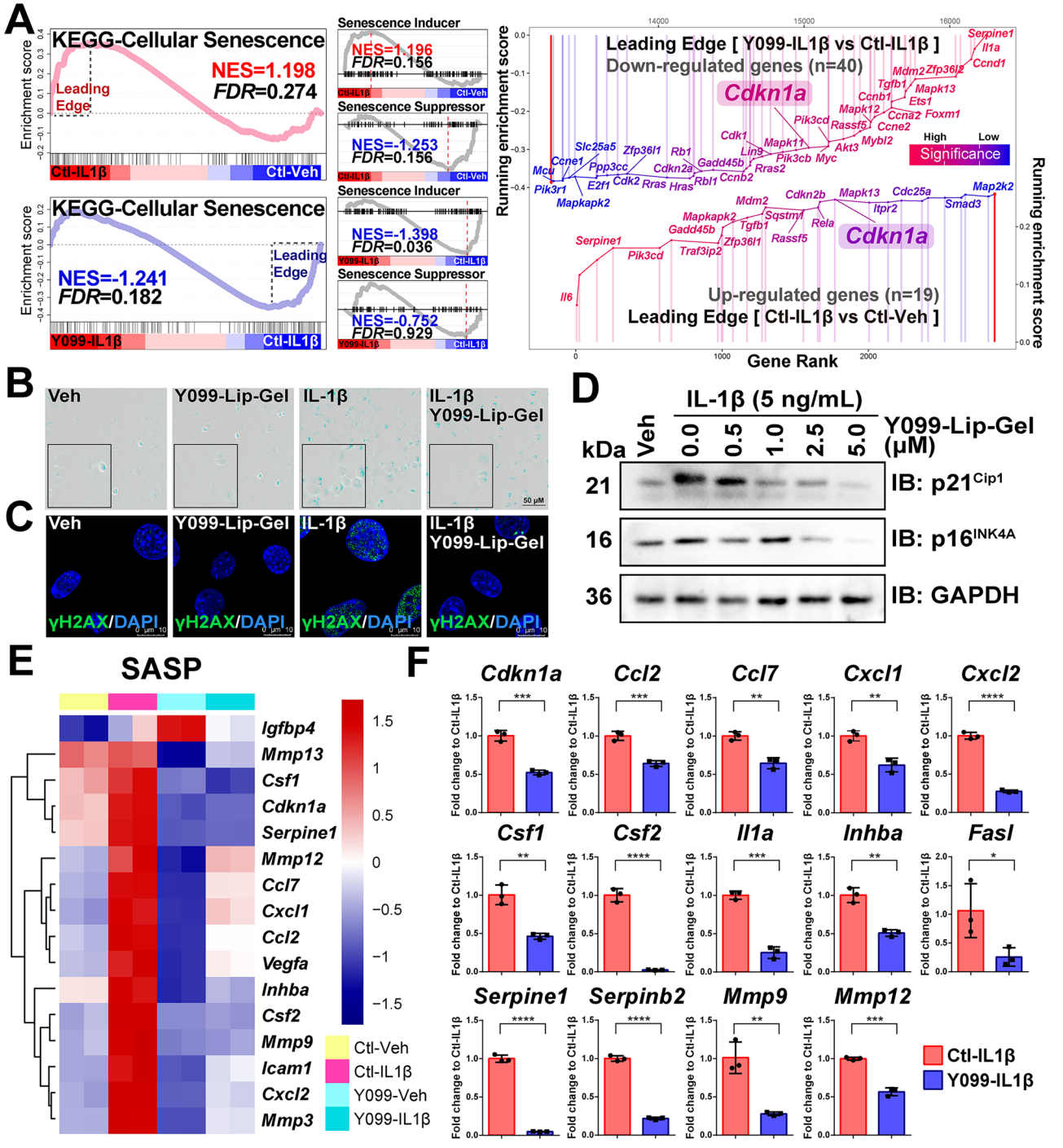

Fig. 7 Y099-Lip-Gel suppresses cellular senescence by inhibiting senescence inducers and the senescence-associated secretory phenotype factors. **A** Gene set enrichment analysis (GSEA) of the cellular senescence-related genes. NES, enrichment score normalized to mean enrichment of random samples of the same size. A positive or negative NES indicates that the genes enriched in the gene set are mostly up-regulated or down-regulated by the perturbations. FDR, *p* value estimated by one-way ANOVA and adjusted by Benjamini–Hochberg method. FDR < 0.25 is considered significant. The leading-edge subset is considered the main genes contributing to the difference between the compared groups. **B** β-galactosidase staining showing the senescent chondrocytes. **C** Immunofluorescence staining of γH2AX indicating the DNA damage in chondrocytes. **D** Western blot analyses of the protein abundance of senescence indicators $P21^{Cip1}$ and $P16^{INK4A}$ in the vehicle-induced or IL-1β-induced chondrocytes treated with or without Y099-Lip-Gel (Y099: 5 μM) for 24 h. **E** Heatmap showing the expression of *Cdkn1a* and the rescued senescence-associated secretory phenotype (SASP) factors ($n = 15$). **F** qPCR validations of *Cdkn1a* and the rescued SASP factors in IL-1β-induced chondrocytes treated with or without Y099-Lip-Gel (Y099: 5 μM) for 24 h. Data represent mean ± SD; $N = 3$/group; $^{*}P < 0.05$, $^{**}P < 0.01$, $^{***}P < 0.001$, $^{****}P < 0.0001$ by Student's *t*-test

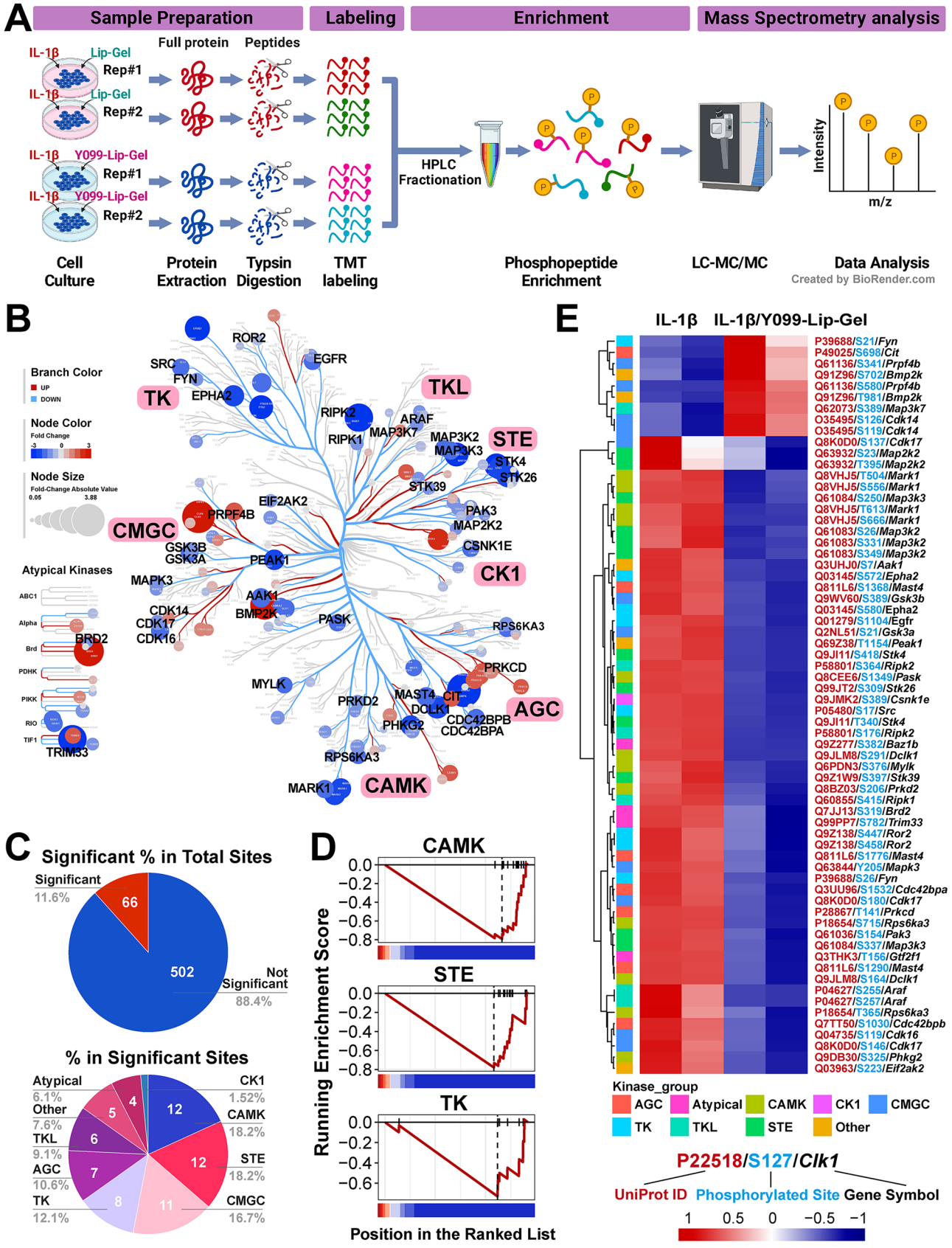
A
Sample Preparation
Labeling
Enrichment
Mass Spectrometry analysis
IL-1β Lip-Gel Rep#1
IL-1β Lip-Gel Rep#2
IL-1β Y099-Lip-Gel Rep#1
IL-1β Y099-Lip-Gel Rep#2
Full protein
Peptides
HPLC Fractionation
Intensity
m/z
Cell Culture
Protein Extraction
Trypsin Digestion
TMT labeling
Phosphopeptide Enrichment
LC-MC/MC
Data Analysis
Created by BioRender.com
B
Branch Color
UP
DOWN
Node Color
Fold Change
Node Size
Fold-Change Absolute Value
Atypical Kinases
TK
TKL
STE
CMGC
CK1
AGC
CAMK
ROR2
EGFR
SRC
FYN
EPHA2
RIPK2
ARAF
RIPK1
MAP3K7
MAP3K2
MAP3K3
STK4
STK26
STK39
EIF2AK2
PRPF4B
PAK3
MAP2K2
CSNK1E
GSK3B
GSK3A
PEAK1
MAPK3
AAK1
BMP2K
CDK14
CDK17
CDK16
PASK
RPS6KA3
PRKCD
MYLK
PRKD2
MAST4
CIT
DCLK1
CDC42BPB
CDC42BPA
PHKG2
RPS6KA3
MARK1
ABC1
Alpha
Brd
PDHK
PIKK
RIO
TIF1
BRD2
TRIM33
E
IL-1β IL-1β/Y099-Lip-Gel
P39688/S21/Fyn
P49025/S698/Cit
Q61136/S341/Prpf4b
Q91Z96/S702/Bmp2k
Q61136/S580/Prpf4b
Q91Z96/T981/Bmp2k
Q62073/S389/Map3k7
O35495/S126/Cdk14
O35495/S119/Cdk14
Q8K0D0/S137/Cdk17
Q63932/S23/Map2k2
Q63932/T395/Map2k2
Q8VHJ5/T504/Mark1
Q8VHJ5/S556/Mark1
Q61084/S250/Map3k3
Q8VHJ5/T613/Mark1
Q8VHJ5/S666/Mark1
Q61083/S26/Map3k2
Q61083/S331/Map3k2
Q61083/S349/Map3k2
Q3UHJ0/S7/Aak1
Q03145/S572/Epha2
Q811L6/S1368/Mast4
Q9WV60/S389/Gsk3b
Q03145/S580/Epha2
Q01279/S1104/Egfr
Q2NL51/S21/Gsk3a
Q69Z38/T1154/Peak1
Q9JI11/S418/Stk4
P58801/S364/Ripk2
Q8CEE6/S1349/Pask
Q99JT2/S309/Stk26
Q9JMK2/S389/Csnk1e
P05480/S17/Src
Q9JI11/T340/Stk4
P58801/S176/Ripk2
Q9Z277/S382/Baz1b
Q9JLM8/S291/Dclk1
Q6PDN3/S376/Mylk
Q9Z1W9/S397/Stk39
Q8BZ03/S206/Prkd2
Q60855/S415/Ripk1
Q7JJ13/S319/Brd2
Q99PP7/S782/Trim33
Q9Z138/S447/Ror2
Q9Z138/S458/Ror2
Q811L6/S1776/Mast4
Q63844/Y205/Mapk3
P39688/S26/Fyn
Q3UU96/S1532/Cdc42bpa
Q8K0D0/S180/Cdk17
P28867/T141/Prkcd
P18654/S715/Rps6ka3
Q61036/S154/Pak3
Q61084/S337/Map3k3
Q3THK3/T156/Gtf2f1
Q811L6/S1290/Mast4
Q9JLM8/S164/Dclk1
P04627/S255/Araf
P04627/S257/Araf
P18654/T365/Rps6ka3
Q7TT50/S1030/Cdc42bpb
Q04735/S119/Cdk16
Q8K0D0/S146/Cdk17
Q9DB30/S325/Phkg2
Q03963/S223/Eif2ak2
Kinase_group
AGC
Atypical
CAMK
CK1
CMGC
TK
TKL
STE
Other
P22518/S127/Clk1
UniProt ID
Phosphorylated Site
Gene Symbol
1 0.5 0 −0.5 −1
C
Significant % in Total Sites
Significant
11.6%
66
502
Not Significant
88.4%
% in Significant Sites
Atypical
6.1%
Other
7.6%
TKL
9.1%
AGC
10.6%
TK
12.1%
CK1
1.52%
CAMK
18.2%
STE
18.2%
CMGC
16.7%
4
5
6
7
8
12
12
11
D
CAMK
STE
TK
Running Enrichment Score
0.0
−0.2
−0.4
−0.6
−0.8
Position in the Ranked List

◂**Fig. 8** Y099-Lip-Gel exerts a significant influence on phosphoproteomics and regulates phosphorylation modification of multiple kinase families. **A** Schematic diagram of phosphoproteomics analysis. The phosphorylated peptides of the vehicle-induced or IL-1β-induced chondrocytes treated with or without Y099-Lip-Gel (Y099: 5 μM) for 24 h were subjected to liquid chromatography-tandem mass spectrometry (LC–MS/MS). **B** Kinome tree showing the kinases with differentially modified phosphosites induced by Y099-Lip-Gel. The kinases with enhanced or suppressed phosphosites were indicated by the red or blue dots. The significant kinases were labeled by official gene symbols in bold. AGC: PKA, PKG, PKC families; CAMK: calcium-/calmodulin-dependent protein kinase; CK1: casein kinase 1; CMGC: CDK, MAPK, GSK3, CLK families; STE: homologs of yeast sterile 7, sterile 11, sterile 20 kinases; TK: tyrosine kinase; TKL: tyrosine kinase-like. **C** Pie charts showing the statistics of the significant phosphosites and the significant phosphosites in each kinase family. **D** Gene set enrichment analysis showing that the phosphorylation of CAMK, STE, and TK families was significantly suppressed by Y099-Lip-Gel. **E** Heatmap showing the 66 phosphosites significantly modified by Y099-Lip-Gel

pathways (e.g., inflammation response, cytokine production), stress pathway (e.g., response to oxidative stress), cartilage homeostasis (e.g., cartilage development, chondrocyte differentiation), bone homeostasis (e.g., ossification, osteoblast differentiation), and protein kinase activity (e.g., regulation of protein serine/threonine kinase activity, negative regulation of phosphorylation) were identified by GO analyses (Fig. 6G). Moreover, KEGG analyses showed that the rescued genes were related to OA-related signaling pathways, such as TNF, IL-17, NF-κB, and MAPK signaling pathways. Of note, KEGG analyses also indicated that cellular senescence was significantly associated with the effect of Y099-Lip-Gel on transcriptome (Fig. 6G).

3.5 Y099-Lip-Gel suppresses cellular senescence by inhibiting senescence inducers and the senescence-associated secretory phenotype factors

Due to the findings of transcriptome strongly suggesting the connection between Y099-Lip-Gel and cellular senescence, the senescence-related gene sets were further investigated by bioinformatics. GSEA showed that IL-1β had the potential in promoting senescence-related genes, whereas Y099-Lip-Gel had a suppressive effect on them (Fig. 7A). Moreover, IL-1β significantly activated senescence inducers and inhibited the senescence suppressors (Fig. 7A). Although Y099-Lip-Gel showed moderate effects on senescence suppressors, it notably inhibited the expression of senescence inducers (FDR < 0.05) (Fig. 7A). Leading edge analyses showed the senescence-related genes significantly up-regulated by IL-1β but down-regulated by Y099-Lip-Gel (Fig. 7A). Of note, senescence inducer *Serpine1* was the top 2 in the leading edge of IL-1β and the top 1 in the leading edge of Y099-Lip-Gel, indicating its critical role in the mechanism of Y099-Lip-Gel against OA (Fig. 7A). To validate whether Y099-Lip-Gel suppresses senescence, β-galactosidase staining was performed, which showed that Y099-Lip-Gel reduced IL-1β-induced senescence of chondrocytes (Fig. 7B). The IF of γH2AX showed that Y099-Lip-Gel decreased IL-1β-induced elevation of γH2AX abundance in nuclei, suggesting that IL-1β-induced DNA damage was rescued by Y099-Lip-Gel (Fig. 7C). The suppression of Y099-Lip-Gel on senescence indicators $P21^{Cip1}$ and $P16^{INK4A}$ was further validated by western blot (Fig. 7D). Moreover, the expression of *Cdkn1a* and the rescued SASP factors ($n = 15$) were characterized (Fig. 7E) and validated by qPCR (Fig. 7F). These findings suggested that Y099-Lip-Gel suppresses senescence by inhibiting senescence inducers and the SASP factors.

3.6 Y099-Lip-Gel has a significant influence on phosphoproteomics and inhibits MAPK and NF-κB signaling activations

Phosphoproteomics analysis was performed to reveal the effects of Y099-Lip-Gel on the kinome (Fig. 8A). As shown in Fig. 8B and C, 568 phosphosites of 155 kinases are identified in chondrocytes, among which 66 phosphosites of 44 kinases were significantly regulated by Y099-Lip-Gel. Moreover, according to the significant phosphosite number, the top 5 kinase categories are CAMK (18.2%), STE (18.2%), CMGC (16.7%), and TK (12.1%) (Fig. 8C). Since the kinome tree did not show the tendency of Y099-Lip-Gel among kinase categories (Fig. 8B), GSEA was employed to determine which categories were polarized by Y099-Lip-Gel. As shown in Fig. 8D, the phosphorylation of CAMK, STE, and TK was significantly suppressed by Y099-Lip-Gel. Among the 66 phosphosites, only 9 phosphosites (13.6%) in 6 kinases, including *Fyn*, *Cit*, *Prpf4b*, *Bmp2k*, *Map3k7*, and *Cdk14*, were subjected to enhanced phosphorylation, whereas most of them (86.4%) was suppressed by Y099-Lip-Gel (Fig. 8E). Of note, according to the perturbation amplitudes of phosphorylation, the top 15 suppressed kinases included *Ripk2* (TKL), *Stk4* (STE), *Dclk1* (CAMK), *Stk26* (STE), *Baz1b* (Atypical), *Epha2* (TK), *Phkg2* (CAMK), *Peak1* (Other), *Aak1* (Other), *Mark1* (CAMK), *Gsk3a* (CMGC), *Cdc42bpb* (AGC), *Mast4* (AGC), *Src* (TK), and *Csnk1e* (CK1) (Fig. 8E). To investigate the function of the significantly regulated kinases, GO analysis was performed, which showed that they are related to stress-activated MAPK cascade, regulation of MAP kinase activity, ERK1 and ERK2 cascade, JNK cascade, activation of MAPK activity, positive regulation of I-kappaB kinase/NF-kappaB signaling, regulation of JNK cascade, and I-kappaB kinase/NF-kappaB signaling (Fig. 9A), suggesting that Y099-Lip-Gel inhibits MAPK and NF-κB signaling activations. Moreover, the pathways associated with aging, senescence, oxidative stress, catabolic process, and IL-1 and IL-6 response were indicated by GO analysis (Fig. 9A). Of note, *Ripk2* and *Ripk1*

showed a high-degree connection with the enriched pathways (Fig. 9A). Western blot further validated that Y099-Lip-Gel suppressed the phosphorylation of ERK1/2, JNK, P65, and IKKα/β induced by IL-1β (Fig. 9B).

3.7 Y099-Lip-Gel exhibits a therapeutic effect on human OA cartilage by promoting aggrecan and suppressing MMP-13 and senescence makers

To explore whether Y099-Lip-Gel has therapeutic effects on human OA cartilage, human OA cartilage explants were harvested from the medial femoral condyle of TKA patients and subjected to Y099-Lip-Gel treatment (Fig. 10A). The cartilage explants from the same patients were divided into two, which were maintained in the IL-1β-contained culture medium to preserve the gene expression of OA phenotypes and treated with or without Y099-Lip-Gel for 48 h, respectively (Fig. 10A). As shown in Fig. 10B, the cartilage explants are around $5 \times 5 \times 5$ mm^3 with a complete cartilage-subchondral bone structure (~ 2 mm cartilage and ~ 3 mm subchondral bone in thickness). Safranin O-fast green staining showed OA-related histological characteristics, such as the loss of the cartilage content and chondrocytes and the wear of the cartilage surface (Fig. 10C). To check the effects of Y099-Lip-Gel on anabolism, catabolism, and senescence, the IHC analyses of aggrecan, MMP-13, and $P21^{Cip1}$ were performed, which showed that the Y099-Lip-Gel was efficient to increase the abundance of aggrecan and suppress the expression of MMP-13 and $P21^{Cip1}$ in the human OA cartilage after 48-h treatment (Fig. 10D and E). These findings supported that Y099-Lip-Gel had a therapeutic effect on human OA cartilage by promoting aggrecan and suppressing MMP-13 and senescence-related gene expression.

4 Discussion

In the present study, the nanoliposome-based thermosensitive hydrogel system succeeded in reducing kinase inhibition-induced cytotoxicity, enhancing cellular tolerance to kinome perturbation, and improving the performance of Y099 in promoting anabolism of cartilage. The findings of this study demonstrated that nanoliposomal Y099 has a pronounced effect on promoting anabolism via notably increasing *Sox9* expression and on suppressing catabolism and inflammation, without causing the inhibition of chondrocyte viability. Moreover, this study suggested that nanoliposomal Y099 can attenuate OA cartilage lesions and preserve subchondral bone by rescuing the OA-related transcriptomic perturbation, regulating kimone modifications, and inhibiting cellular senescence and the SASP productions via inhibiting the MAPK and NF-κB signaling pathways. This study demonstrates the potential of Y099 in OA therapy and proposes a promising and novel strategy of senescence elimination via toxicity-exempted kinome perturbations achieved by advanced nanotechnology for OA.

Targeting senescence by nanoscale platforms has been suggested as an effective strategy for OA. Ren et al. reported that ceria nanoparticles could eliminate the senescent synoviocytes in the rat OA model [53]. The thermosensitive hydrogel loaded with hydroxytyrosol-encapsulated chitosan nanoparticles succeeded in suppressing oxidative stress and inflammation and reducing the senescent cells induced by hydrogen peroxide [54]. However, the exact mechanisms by which these nanoparticles eliminate senescence are largely unknown. RNA interference combined with nanoscale delivery platforms has also been shown to reduce chondrocyte senescence and slow the progression of OA. Zhu et al. proposed a novel injectable self-assembling peptide nanofiber hydrogel to deliver aging-related mir-29b-5p, which exhibited the capabilities of senescence elimination, anabolism promotion, catabolism inhibition, and cartilage repair [55]. Moreover, a direct strategy targeting senescence facilitated by p16INK4a siRNA-loaded PLGA nanoparticles was proven to suppress p16INK4a in fibroblast-like synoviocytes [56]. Although the senescence elimination effects of RNA-based strategies have been demonstrated, single miRNA or siRNA targeting might fail since the intracellular RNA regulation network is complicated and dynamic. Compared with the existing studies, the present study is the first to target senescence by a kinome perturbation strategy facilitated by the nanoliposome-loaded hydrogel. Many kinases and related signaling pathways have also been implied in cellular senescence and the SASP productions in OA. Kinome perturbation is a comprehensive strategy modifying a batch of senescence-related kinases, thus widely inhibiting the expression of the downstream senescence-related genes.

Current protein kinase inhibitors, which have been developed since 2001 when the first tyrosine kinase inhibitor imatinib was approved for chronic myeloid leukemia, are most for cancer therapy [57]. Very few of them, such as tofacitinib and upadacitinib, are approved for skeleton diseases [58, 59]. Although the functions of various protein kinases, such as the MAPK family, have been well-characterized in OA mechanisms [18, 60], no protein kinase inhibitors have been approved for OA therapy. The insufficient selectivity and off-target toxicity of kinase inhibitors, which are caused by the sequence and structural similarities shared by protein kinase families [61], hinder the development of protein kinase inhibitors. The challenges also include the toxicity facilitated by elevated lipophilicity which causes the binding to adventitious targets [62]. Rationally designed nanoplatforms have strength in sustained and controlled release of the drug, thus enhancing the bioavailability and reducing the dose-related toxicity [28, 63]. Nanoliposomes are biocompatible, biodegradable, low toxic, and site-specific for both

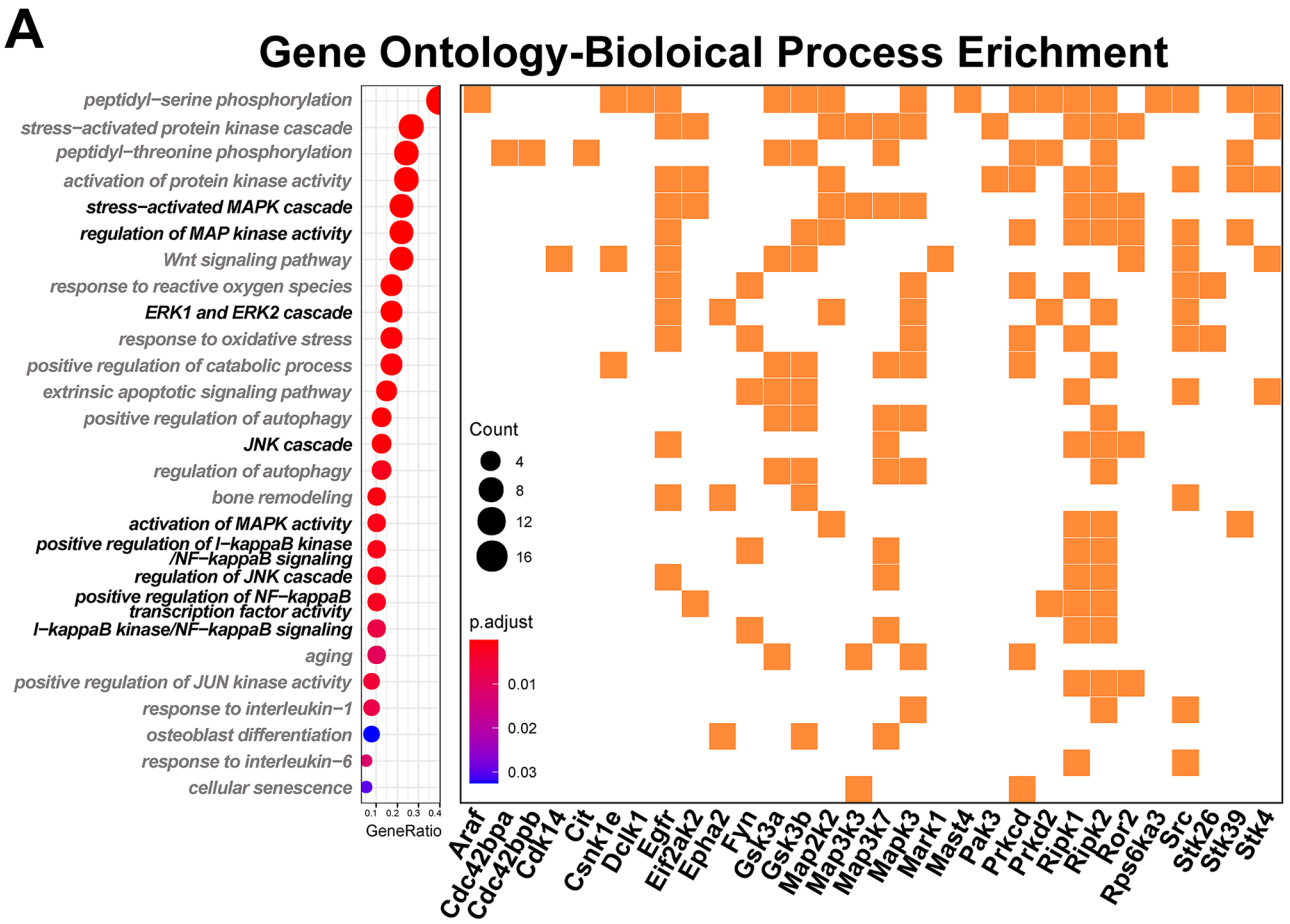

Fig. 9 Y099-Lip-Gel inhibits MAPK and NF-κB signaling activations. **A** Gene ontology analysis showing the pathways significantly related to differentially modified phosphosites induced by Y099-Lip-Gel and the kinases enriched in these pathways. The MAPK and NF-κB signaling-related pathways are labeled in bold in the right dot plot. GeneRatio indicates the kinase number ratio in each GO item. The color and size of the dot represent the *P* value adjusted by Benjamini and Hochberg method (FDR) and the gene number assigned to the corresponding GO item, respectively. The kinases related to significant pathways are shown in the right heatmap and represented by official gene symbols. **B** Western blot analyses of the phosphorylation of MAPK and NF-κB signaling in the vehicle-induced or IL-1β-induced chondrocytes treated with or without Y099-Lip-Gel (Y099: 5 μM) for 24 h

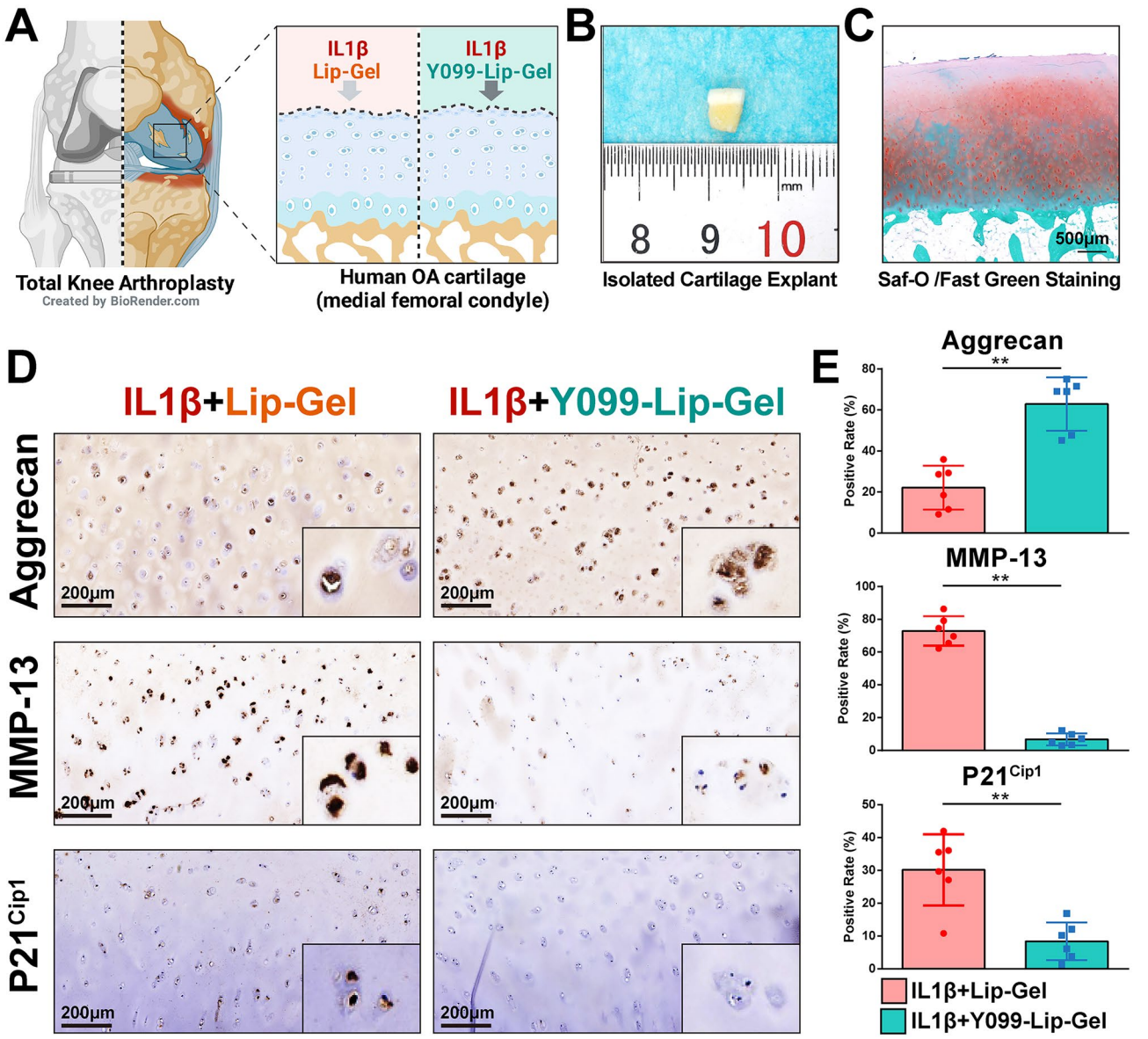

Fig. 10 Y099-Lip-Gel exhibits a therapeutic effect on human OA cartilage explants by promoting aggrecan and suppressing MMP-13 and P21^{Cip1} expression. **A** Schematic diagram showing the procedures of the human OA cartilage explant harvest and drug treatments. The human OA cartilage explants were harvested from the medial condyle of the femur from the OA patients undergoing total knee arthroplasty. **B** Image of the isolated human OA cartilage explant. **C** Safranin O-fast green staining of OA cartilage explant. Scar bar: 500 μm. **D** Representative images of immunohistochemistry analyses of the protein abundance of the anabolic indicator aggrecan, catabolic indicator MMP-13, and senescence indicators P21^{Cip1} in the IL-1β (10 ng/mL)-maintained human explants treated with or without Y099-Lip-Gel (Y099: 5 μM) for 48 h. Scar bar: 200 μm. **E** Quantitative analyses of immunohistochemistry. Data represent mean ± SD; $N = 6$/group; $^{**}P < 0.01$ by paired t-test

hydrophilic and hydrophobic drugs [64]. Lecithin is a type of natural phospholipid wildly used for nanoparticle synthesis and drug delivery [65]. The present study utilized lecithin nanoliposomes, which are simple to prepare and effective at reducing drug toxicity while enhancing the beneficial effects of the drug.

The existing treatments used in clinical practices have significant drawbacks, such as gastrointestinal issues caused by systemic administration of nonsteroidal anti-inflammatory drugs and the lack of clarity regarding the effectiveness of intra-articular corticosteroids or hyaluronic acid. Moreover, the low accumulation and retention of drugs in joints resulting from conventional systemic or intra-articular administrations lead to decreased drug efficacy and dose-limiting toxicities. Hydrogels, like the PLGA-PEG-PLGA thermosensitive hydrogels, are beneficial due to their biocompatibility, lack of toxicity, biodegradability, and excellent absorption ability,

which make them an ideal choice for intra-articular drug delivery [64, 66]. The thermosensitive hydrogel in the present study prolonged the retention and release of nanoliposomal Y099, as well as promoted the stability of nanoliposomes. Thus, Y099-Lip-Gel has the potential to be utilized as a novel therapy for the treatment of OA.

Several limitations need to be considered in this study. First, although the injections could retain and work locally in the joint cavity, the delivery system in the present study lacks the targeting effects of cartilage. A composite and pleiotropic drug delivery system with high delivery efficiency and specific targeting ability is expected to further improve Y099-Lip-Gel. Secondly, the mechanical properties of Y099-Lip-Gel were not assessed in this study. More efforts are needed to develop a physical-activity-adapted and mechanic-resistant hydrogel to improve its therapeutic effects. Moreover, since the effects of Y099-Lip-Gel on the other joint elements were not assessed, whether Y099-Lip-Gel affected them remained unclear. Finally, although histological assessments of key organs were performed for the evaluation of systemic toxicity, the complete blood count and biochemical indicators of peripheral blood were absent.

5 Conclusions

Nanoliposomal Y099-loaded thermosensitive hydrogel rescues the OA-related transcriptome and regulates kinome modifications to suppress catabolism, promote anabolism, and eliminate cellular senescence. Nanoliposomal Y099-loaded thermosensitive hydrogel is simple to prepare, effective at reducing drug toxicity, prolonging retention and release, promoting stability, and enhancing the beneficial effects of the drug; thus, it has the potential to be a novel therapeutic agent for OA. Nanoliposome-based hydrogel system has strength in reducing kinase inhibition-induced cytotoxicity, enhancing cellular tolerance to kinome perturbation, and improving the performance of protein kinase inhibitors. Senescence elimination via toxicity-exempted kinome perturbations achieved by advanced nanotechnology is a promising strategy for OA.

Supplementary Information The online version contains supplementary material available at https://doi.org/10.1007/s42114-023-00673-w.

Author contributions Junlai Wan: investigation (cell experiments and human explant study), methodology, data curation, writing – review & editing; Zhiyi He: investigation (cell experiments and animal study), data curation, writing – review & editing; Yingchao Zhao: conceptualization, methodology, writing – original draft (supplementary); Xiaoxia Hao: data curation; Jiarui Cui: visualization (graphical illustrations); Anmin Chen: supervision, funding acquisition; Jun Zhou: conceptualization, project administration, investigation (preparation, synthesis, analyses of nanoscale drug), supervision, resources, funding acquisition, data curation, writing – original draft (supplementary); J. Zhang: conceptualization, project administration, methodology, investigation (histomorphometric analyses, transcriptomic and phosphoproteomic analyses, bioinformatic analyses, statistics), data curation, visualization (all the figures), writing – original draft (main). All authors listed have made a substantial, direct, and intellectual contribution to the work and approved it for publication.

Funding This study was supported by Grants-in-Aid for Research Activity Start-up (Grant No. 19K24154) from Japan Society for the Promotion of Science (Jun Zhou) and the National Natural Science Foundation of China (Grant No. 81902262) (Anmin Chen).

Data availability The data are available from the corresponding author upon reasonable request.

Declarations

Conflict of interest The authors declare no competing interests.

References

1. Hunter DJ, Bierma-Zeinstra S (2019) Osteoarthritis. Lancet 393(10182):1745–1759
2. Zhou J, He Z, Cui J, Liao X, Cao H, Shibata Y, Miyazaki T, Zhang J (2022) Identification of mechanics-responsive osteocyte signature in osteoarthritis subchondral bone. Bone Joint Res 11(6):362–370
3. Hernandez-Segura A, Nehme J, Demaria M (2018) Hallmarks of cellular senescence. Trends Cell Biol 28(6):436–453
4. Coryell PR, Diekman BO, Loeser RF (2021) Mechanisms and therapeutic implications of cellular senescence in osteoarthritis. Nat Rev Rheumatol 17(1):47–57
5. Cui J, Shibata Y, Zhu T, Zhou J, Zhang J (2022) Osteocytes in bone aging: advances, challenges, and future perspectives. Ageing Res Rev 77
6. Huang W, Hickson LJ, Eirin A, Kirkland JL, Lerman LO (2022) Cellular senescence: the good, the bad and the unknown. Nat Rev Nephrol 18(10):611–627
7. Zhang H, Cao X, Tang M, Zhong G, Si Y, Li H, Zhu F, Liao Q, Li L, Zhao J et al (2021)A subcellular map of the human kinome. Elife 10
8. Zarrin AA, Bao K, Lupardus P, Vucic D (2021) Kinase inhibition in autoimmunity and inflammation. Nat Rev Drug Discov 20(1):39–63
9. Amirthalingam M, Palanisamy S, Tawata S (2021) p21-Activated kinase 1 (PAK1) in aging and longevity: An overview. Ageing Res Rev 71
10. Ayala-Aguilera CC, Valero T, Lorente-Macias A, Baillache DJ, Croke S, Unciti-Broceta A (2022) Small molecule kinase inhibitor drugs (1995–2021): medical indication, pharmacology, and synthesis. J Med Chem 65(2):1047–1131

11. Guo Q, Chen X, Chen J, Zheng G, Xie C, Wu H, Miao Z, Lin Y, Wang X, Gao W et al (2021) STING promotes senescence, apoptosis, and extracellular matrix degradation in osteoarthritis via the NF-kappaB signaling pathway. Cell Death Dis 12(1):13
12. Weng PW, Pikatan NW, Setiawan SA, Yadav VK, Fong IH, Hsu CH, Yeh CT, Lee WH (2022)Role of GDF15/MAPK14 axis in chondrocyte senescence as a novel senomorphic agent in osteoarthritis. Int J Mol Sci 23(13)
13. Novikov FN, Panova MV, Titov IY, Stroylov VS, Stroganov OV, Chilov GG (2021) Inhibition of SYK and cSrc kinases can protect bone and cartilage in preclinical models of osteoarthritis and rheumatoid arthritis. Sci Rep 11(1):23120
14. Wei Y, Luo L, Gui T, Yu F, Yan L, Yao L, Zhong L, Yu W, Han B, Patel JM et al (2021)Targeting cartilage EGFR pathway for osteoarthritis treatment. Sci Transl Med 13(576)
15. Wein MN, Liang Y, Goransson O, Sundberg TB, Wang J, Williams EA, O'Meara MJ, Govea N, Beqo B, Nishimori S et al (2016) SIKs control osteocyte responses to parathyroid hormone. Nat Commun 7:13176
16. Tang CC, Castro Andrade CD, O'Meara MJ, Yoon SH, Sato T, Brooks DJ, Bouxsein ML, Martins JDS, Wang J, Gray NS et al (2021)Dual targeting of salt inducible kinases and CSF1R uncouples bone formation and bone resorption. Elife 10
17. Hu W, Chen Y, Dou C, Dong S (2021) Microenvironment in subchondral bone: predominant regulator for the treatment of osteoarthritis. Ann Rheum Dis 80(4):413–422
18. Ferrao Blanco MN, Domenech Garcia H, Legeai-Mallet L, van Osch G (2021) Tyrosine kinases regulate chondrocyte hypertrophy: promising drug targets for Osteoarthritis. Osteoarthritis Cartilage 29(10):1389–1398
19. Tarumoto Y, Lin S, Wang J, Milazzo JP, Xu Y, Lu B, Yang Z, Wei Y, Polyanskaya S, Wunderlich M et al (2020) Salt-inducible kinase inhibition suppresses acute myeloid leukemia progression in vivo. Blood 135(1):56–70
20. Li F, Li Q, Kimura H, Xie X, Zhang X, Wu N, Sun X, Xu BB, Algadi H, Pashameah RA et al (2023) Morphology controllable urchin-shaped bimetallic nickel-cobalt oxide/carbon composites with enhanced electromagnetic wave absorption performance. J Mater Sci Technol 148:250–259
21. Hou C, Yang W, Kimura H, Xie X, Zhang X, Sun X, Yu Z, Yang X, Zhang Y, Wang B et al (2023) Boosted lithium storage performance by local build-in electric field derived by oxygen vacancies in 3D holey N-doped carbon structure decorated with molybdenum dioxide. J Mater Sci Technol 142:185–195
22. Mu Q, Liu R, Kimura H, Li J, Jiang H, Zhang X, Yu Z, Sun X, Algadi H, Guo Z et al (2022) Supramolecular self-assembly synthesis of hemoglobin-like amorphous CoP@N, P-doped carbon composites enable ultralong stable cycling under high-current density for lithium-ion battery anodes. Adv Compos Hybrid Mater 6(1):23
23. Hou C, Wang B, Murugadoss V, Vupputuri S, Chao Y, Guo Z, Wang C, Du W (2020) Recent advances in Co3O4 as anode materials for high-performance lithium-ion batteries. Eng Sci 11:19–30
24. Yang W, Peng D, Kimura H, Zhang X, Sun X, Pashameah RA, Alzahrani E, Wang B, Guo Z, Du W et al (2022) Honeycomb-like nitrogen-doped porous carbon decorated with Co3O4 nanoparticles for superior electrochemical performance pseudo-capacitive lithium storage and supercapacitors. Adv Compos Hybrid Mater 5(4):3146–3157
25. Dang C, Mu Q, Xie X, Sun X, Yang X, Zhang Y, Maganti S, Huang M, Jiang Q, Seok I et al (2022) Recent progress in cathode catalyst for nonaqueous lithium oxygen batteries: a review. Adv Compos Hybrid Mater 5(2):606–626
26. Ma Y, Xie X, Yang W, Yu Z, Sun X, Zhang Y, Yang X, Kimura H, Hou C, Guo Z et al (2021) Recent advances in transition metal oxides with different dimensions as electrodes for high-performance supercapacitors. Adv Compos Hybrid Mater 4(4):906–924
27. Kim BY, Rutka JT, Chan WC (2010) Nanomedicine. N Engl J Med 363(25):2434–2443
28. Al-Lawati H, Binkhathlan Z, Lavasanifar A (2019) Nanomedicine for the effective and safe delivery of non-steroidal anti-inflammatory drugs: a review of preclinical research. Eur J Pharm Biopharm 142:179–194
29. Lu W, Yao J, Zhu X, Qi Y (2021) Nanomedicines: redefining traditional medicine. Biomed Pharmacother 134
30. Jin GZ (2020)Current nanoparticle-based technologies for osteoarthritis therapy. Nanomaterials (Basel) 10(12)
31. Seo BB, Kwon Y, Kim J, Hong KH, Kim SE, Song HR, Kim YM, Song SC (2022) Injectable polymeric nanoparticle hydrogel system for long-term anti-inflammatory effect to treat osteoarthritis. Bioact Mater 7:14–25
32. Yin M, Zhang J, Zeng X, Zhang H, Gao Y (2021) Target identification and drug discovery by data-driven hypothesis and experimental validation in ovarian endometriosis. Fertil Steril 116(2):478–492
33. Liang S, Lv ZT, Zhang JM, Wang YT, Dong YH, Wang ZG, Chen K, Cheng P, Yang Q, Guo FJ et al (2018) Necrostatin-1 attenuates trauma-induced mouse osteoarthritis and IL-1beta induced apoptosis via HMGB1/TLR4/SDF-1 in primary mouse chondrocytes. Front Pharmacol 9:1378
34. Kim GW, Han MS, Park HR, Lee EJ, Jung YK, Usmani SE, Ulici V, Han SW, Beier F (2015) CXC chemokine ligand 12a enhances chondrocyte proliferation and maturation during endochondral bone formation. Osteoarthritis Cartilage 23(6):966–974
35. Livak KJ, Schmittgen TD (2001) Analysis of relative gene expression data using real-time quantitative PCR and the 2(-delta delta C(T)) method. Methods 25(4):402–408
36. Zhang J, Hao X, Chi R, Qi J, Xu T (2021) Moderate mechanical stress suppresses the IL-1beta-induced chondrocyte apoptosis by regulating mitochondrial dynamics. J Cell Physiol 236(11):7504–7515
37. Ao Y, Wu Z, Liao Z, Lan J, Zhang J, Sun P, Liu B, Wang Z (2023) Role of C-terminal phosphorylation of lamin A in DNA damage and cellular senescence. Cells 12(4)
38. Zhang J, Hao X, Chi R, Liu J, Shang X, Deng X, Qi J, Xu T (2022) Whole transcriptome mapping identifies an Immune- and metabolism-related non-coding RNA Landscape remodeled by mechanical stress in IL-1beta-induced rat OA-like chondrocytes. Front Genet 13
39. Love MI, Huber W, Anders S (2014) Moderated estimation of fold change and dispersion for RNA-seq data with DESeq2. Genome Biol 15(12):550
40. Kolde R, Laur S, Adler P, Vilo J (2012) Robust rank aggregation for gene list integration and meta-analysis. Bioinformatics 28(4):573–580
41. Yu G, Wang LG, Han Y, He QY (2012) clusterProfiler: an R package for comparing biological themes among gene clusters. OMICS 16(5):284–287
42. Avelar RA, Ortega JG, Tacutu R, Tyler EJ, Bennett D, Binetti P, Budovsky A, Chatsirisupachai K, Johnson E, Murray A et al (2020) A multidimensional systems biology analysis of cellular senescence in aging and disease. Genome Biol 21(1):91
43. Liu F, Gai X, Wu Y, Zhang B, Wu X, Cheng R, Tang B, Shang K, Zhao N, Deng W et al (2022) Oncogenic beta-catenin stimulation of AKT2-CAD-mediated pyrimidine synthesis is targetable vulnerability in liver cancer. Proc Natl Acad Sci U S A 119(39)
44. Xiao J, Zhang L, Yi H, Zou L, Mo J, Xue F, Zheng J, Huang Y, Lu H, Wu H et al (2022) Inhibiting ALK-TOPK signaling pathway promotes cell apoptosis of ALK-positive NSCLC. Cell Death Dis 13(9):828
45. Manteca A, Sanchez J, Jung HR, Schwammle V, Jensen ON (2010) Quantitative proteomics analysis of Streptomyces coelicolor development demonstrates that onset of secondary metabolism coincides with hypha differentiation. Mol Cell Proteomics 9(7):1423–1436

46. Metz KS, Deoudes EM, Berginski ME, Jimenez-Ruiz I, Aksoy BA, Hammerbacher J, Gomez SM, Phanstiel DH (2018)Coral: clear and customizable visualization of human kinome data. Cell Syst 7(3):347–350 e341
47. Hao X, Zhang J, Shang X, Sun K, Zhou J, Liu J, Chi R, Xu T (2022) Exercise modifies the disease-relevant gut microbial shifts in post-traumatic osteoarthritis rats. Bone Joint Res 11(4):214–225
48. Glasson SS, Chambers MG, Van Den Berg WB, Little CB (2010) The OARSI histopathology initiative - recommendations for histological assessments of osteoarthritis in the mouse. Osteoarthritis Cartilage 18(Suppl 3):S17-23
49. Mankin HJ, Johnson ME, Lippiello L (1981)Biochemical and metabolic abnormalities in articular cartilage from osteoarthritic human hips. III. Distribution and metabolism of amino sugar-containing macromolecules. J Bone Joint Surg Am 63(1):131–139
50. McNulty MA, Loeser RF, Davey C, Callahan MF, Ferguson CM, Carlson CS (2011) A comprehensive histological assessment of osteoarthritis lesions in mice. Cartilage 2(4):354–363
51. Lotinun S, Ishihara Y, Nagano K, Kiviranta R, Carpentier VT, Neff L, Parkman V, Ide N, Hu D, Dann P et al (2019) Cathepsin K-deficient osteocytes prevent lactation-induced bone loss and parathyroid hormone suppression. J Clin Invest 129(8):3058–3071
52. Cui J, Shibata Y, Itaka K, Zhou J, Zhang J (2022) Unbiased comparison and modularization identify time-related transcriptomic reprogramming in exercised rat cartilage: integrated data mining and experimental validation. Front Physiol 13
53. Ren X, Zhuang H, Jiang F, Zhang Y, Zhou P (2023)Ceria Nanoparticles alleviated osteoarthritis through attenuating senescence and senescence-associated secretory phenotype in synoviocytes. Int J Mol Sci 24(5)
54. Valentino A, Conte R, De Luca I, Di Cristo F, Peluso G, Bosetti M, Calarco A (2022)Thermo-responsive gel containing hydroxytyrosol-chitosan nanoparticles (Hyt@tgel) counteracts the increase of osteoarthritis biomarkers in human chondrocytes. Antioxidants (Basel) 11(6)
55. Zhu J, Yang S, Qi Y, Gong Z, Zhang H, Liang K, Shen P, Huang YY, Zhang Z, Ye W et al (2022)Stem cell-homing hydrogel-based miR-29b-5p delivery promotes cartilage regeneration by suppressing senescence in an osteoarthritis rat model. Sci Adv8(13):eabk0011
56. Park H, Lee HR, Shin HJ, Park JA, Joo Y, Kim SM, Beom J, Kang SW, Kim DW, Kim J (2022) p16INK4a-siRNA nanoparticles attenuate cartilage degeneration in osteoarthritis by inhibiting inflammation in fibroblast-like synoviocytes. Biomater Sci 10(12):3223–3235
57. Cohen P, Cross D, Janne PA (2021) Kinase drug discovery 20 years after imatinib: progress and future directions. Nat Rev Drug Discov 20(7):551–569
58. Dhillon S (2017) Tofacitinib: a review in rheumatoid arthritis. Drugs 77(18):1987–2001
59. Rubbert-Roth A, Enejosa J, Pangan AL, Haraoui B, Rischmueller M, Khan N, Zhang Y, Martin N, Xavier RM (2020) Trial of upadacitinib or abatacept in rheumatoid arthritis. N Engl J Med 383(16):1511–1521
60. Fukui T, Yik JHN, Doyran B, Davis J, Haudenschild AK, Adamopoulos IE, Han L, Haudenschild DR (2021) Bromodomain-containing-protein-4 and cyclin-dependent-kinase-9 inhibitors interact synergistically in vitro and combined treatment reduces post-traumatic osteoarthritis severity in mice. Osteoarthritis Cartilage 29(1):68–77
61. Moran G, Elaine A (2021)Protein kinase inhibitors - selectivity or toxicity? In: Protein Kinases. edn. Edited by Rajesh Kumar S. Rijeka: IntechOpen Ch. 2
62. Roskoski R Jr (2023) Properties of FDA-approved small molecule protein kinase inhibitors: a 2023 update. Pharmacol Res 187
63. Velpurisiva P, Piel BP, Lepine J, Rai P (2018) GSK461364A, a polo-like kinase-1 inhibitor encapsulated in polymeric nanoparticles for the treatment of glioblastoma multiforme (GBM). Bioengineering (Basel)5(4)
64. Singh AP, Biswas A, Shukla A, Maiti P (2019) Targeted therapy in chronic diseases using nanomaterial-based drug delivery vehicles. Signal Transduct Target Ther 4:33
65. Li J, Wang X, Zhang T, Wang C, Huang Z, Luo X, Deng Y (2015) A review on phospholipids and their main applications in drug delivery systems. Asian J Pharm Sci 10(2):81–98
66. Cao H, Duan L, Zhang Y, Cao J, Zhang K (2021) Current hydrogel advances in physicochemical and biological response-driven biomedical application diversity. Signal Transduct Target Ther 6(1):426

Authors and Affiliations

Junlai Wan[1] · Zhiyi He[1] · Yingchao Zhao[2,3] · Xiaoxia Hao[4] · Jiarui Cui[5] · Anmin Chen[1] · Jun Zhou[6,7] · Jiaming Zhang[1]

1 Department of Orthopedics, Tongji Hospital, Tongji Medical College, Huazhong University of Science and Technology, Wuhan 430030, China

2 Institute of Radiation Oncology, Union Hospital, Tongji Medical College, Huazhong University of Science and Technology, 430022 Wuhan, China

3 Cancer Center, Union Hospital, Tongji Medical College, Huazhong University of Science and Technology, 430022 Wuhan, China

4 Department of Rehabilitation, Tongji Hospital, Tongji Medical College, Huazhong University of Science and Technology, Wuhan 430030, China

5 Longhua Hospital, Shanghai University of Traditional Chinese Medicine, Shanghai 200032, China

6 Department of Conservative Dentistry, Division of Biomaterials and Engineering, Showa University School of Dentistry, Tokyo 142-8555, Japan

7 Department of Biofunction Research, Institute of Biomaterials and Bioengineering, Tokyo Medical and Dental University (TMDU), Tokyo 101-0062, Japan